# Evidence for the presence of chondrule- and CAI-derived material in an isotopically anomalous Antarctic micrometeorite

Bastien SOENS [*,1,2], Martin D. SUTTLE [3,4], Ryoga MAEDA[1], Frank VANHAECKE [5], Akira YAMAGUCHI [6], Matthias VAN GINNEKEN [7], Vinciane DEBAILLE[2], Philippe CLAEYS [1], and Steven GODERIS [1]

[1]Analytical-, Environmental-, and Geo-Chemistry, Vrije Universiteit Brussel, Pleinlaan 2, Brussels 1050, Belgium
[2]Laboratoire G-Time, Université Libre de Bruxelles 50, Av. F.D. Roosevelt CP 160/02, Brussels 1050, Belgium
[3]Dipartimento di Scienze della Terra, Università di Pisa, Via S. Maria 53, Pisa 56126, Italy
[4]Planetary Materials Group, Department of Earth Sciences, Natural History Museum, Cromwell Road, London SW7 5BD, UK
[5]Atomic & Mass Spectrometry – A&MS Research Group, Department of Chemistry, Ghent University, Krijgslaan 218 – S12, Ghent 9000, Belgium
[6]National Institute of Polar Research, 10-3 Midori-cho, Tachikawa-shi, Tokyo 190-8518, Japan
[7]Centre for Astrophysics and Planetary Science, University of Kent, Canterbury, Kent CT2 7NZ, UK
*Corresponding author. E-mail: Bastien.Soens@vub.be

Abstract–We report the discovery of a unique, refractory phase-bearing micrometeorite (WF1202A-001) from the Sør Rondane Mountains, East Antarctica. A silicate-rich cosmic spherule (~400 μm) displays a microporphyritic texture containing Ca-Al-rich inclusion (CAI)-derived material (~5–10 area%), including high-Mg forsterite ($Fo_{98-99}$) and enstatite ($En_{98-99}$, $Wo_{0-1}$). The micrometeorite also hosts a spherical inclusion (~209 μm), reminiscent of chondrules, displaying a barred olivine texture. Oxygen isotopic compositions of the micrometeorite groundmass ($\delta^{17}O = -3.46‰$, $\delta^{18}O = 10.43‰$, $\Delta^{17}O = -1.96‰$) are consistent with a carbonaceous chondrite precursor body. Yet, a relict forsterite grain is characterized by $\delta^{17}O = -45.8‰$, $\delta^{18}O = -43.7‰$, $\Delta^{17}O = -23.1‰$, compatible with CAIs. In contrast, a relict low-Ca pyroxene grain ($\delta^{17}O = -4.96‰$, $\delta^{18}O = -4.32‰$, $\Delta^{17}O = -2.71‰$) presumably represents a first-generation silicate grain that accreted $^{18}O$-rich gas or dust in a transient melting scenario. The spherical inclusion displays anomalous oxygen isotope ratios ($\delta^{17}O = -0.98‰$, $\delta^{18}O = -2.16‰$, $\Delta^{17}O = 0.15‰$), comparable to anhydrous interplanetary dust particles (IDPs) and fragments from Comet 81P/Wild2. Based on its major element geochemistry, the chondrule size, and oxygen isotope systematics, micrometeorite WF1202A-001 likely sampled a carbonaceous chondrite parent body similar to, but distinct from CM, CO, or CV chondrites. This observation may suggest that some carbonaceous chondrite bodies can be linked to comets. The reconstructed atmospheric entry parameters of micrometeorite WF1202A-001 suggest that the precursor particle originated from a low-inclination, low-eccentricity source region, most likely either the main belt asteroids or Jupiter family comets (JFCs).

## INTRODUCTION

Chondrules are mm-sized, ferromagnesian objects formed by repeated flash-melting events in the solar nebula (Gooding et al. 1980; Wasson 1993; Hewins 1996; Rubin 2000a). As such, they represent a valuable archive recording the pre-accretionary history of the solar nebula. Various models have previously been proposed to explain chondrule formation, including gamma-ray bursts (McBreen and Hanlon 1999); nebular shock waves (Ciesla and Hood 2002; Desch and Connolly 2002); planetesimal collisions and impacts (Sanders and Scott 2012; Johnson et al. 2015); or, more recently, radiative heating from molten planetesimals or

planetary bodies (Herbst and Greenwood 2016), but none are currently able to fully explain chondrule characteristics. A better understanding of chondrule formation is critical to understand the evolution of the solar system, as chondrules may have played a pivotal role in the development of planetary bodies.

Within chondritic meteorites, chondrules represent one of the three main constituents (up to 80 vol%), along with refractory inclusions (up to 13 vol%), such as CAIs and amoeboid olivine aggregates, and a fine-grained matrix or groundmass (up to 100 vol%). Chondrules display igneous textures, which are commonly subdivided into porphyritic and non-porphyritic subtypes (Gooding et al. 1978). Chondrule textures are mainly determined by two parameters, that is, the physical (e.g., size) and mineralogical characteristics of the precursor material, and second, their subsequent cooling rate from a molten precursor droplet (Lofgren and Russell 1986). For instance, porphyritic chondrules reflect incomplete melting, allowing residual crystals to act as nucleation points for the development of secondary olivine and/or pyroxene crystals (Lofgren 1996; Connolly and Love 1998). These textures have previously been reproduced and verified by numerous lab experiments (e.g., Hewins and Connolly 1996; Lofgren 1996). In contrast, non-porphyritic chondrules display quench textures, including barred olivine, cryptocrystalline, or radial pyroxene patterns. These textures are developed when the precursor material is superheated above the liquidus, destroying all primary crystal nuclei, and subsequently cooled down at highly variable cooling rates (e.g., Connolly and Hewins 1995; Desch and Connolly 2002). Overall, porphyritic chondrules tend to vastly outnumber nonporphyritic subtypes, especially in carbonaceous chondrites (Scott 1988; Kallemeyn et al. 1994; Rubin 2000b; Weisberg et al. 2001; —see also Table 1).

Chondrule fragments have previously been observed in micrometeorites, extraterrestrial dust particles ranging between 10 and 2000 μm in size (Rubin and Grossman 2010; Folco and Cordier 2015), albeit in lower abundances compared to their larger counterpart (e.g., <0.5% in the South Pole Water Well collection—Taylor et al. 2012). As a result, Engrand and Maurette (1998) proposed that micrometeorites may primarily sample a distinct population of "chondrites without chondrules," for example, derived from CI chondrites or another type of chondrule-poor and otherwise unknown extraterrestrial material. According to Genge et al. (2005), this would imply that either (1) meteorites recovered on Earth represent a minor fraction of the supposedly predominant chondrule-poor main belt asteroids, (2) micrometeorites form a strongly biased

Table 1. Average chondrule diameter size (μm) in chondritic meteorites. Note that chondrules may vary in size considerably within different types of chondritic meteorites and that average chondrule sizes are not necessarily representative for specific meteorites. Values reproduced from Scott et al. (1996), McSween (1977), Weisberg et al. (1996, 2001), Grossman et al. (1988), Kallemeyn et al. (1994), Scott (1988), and Rubin (2000b). The "–" symbol indicates the absence of chondrules in CI chondrites and textural data for chondrules in K chondrites.

| Class | Type | Average diameter (μm) | Texture (%por. versus %nonpor.) |
|---|---|---|---|
| Spherical inclusion (WF1202A-001) | | 209 | Barred olivine |
| Carbonaceous | CI | – | – |
| | CM | 300 | 95 – 5 |
| | CO | 150 | 95 – 5 |
| | CR | 700 | 96(98) – 4(2) |
| | CH | 20 | 20 – 80 |
| | CB | 100 – 20.000 | 1 – 99 |
| | CV | 1000 | 94 – 6 |
| | CK | 800 | 99 – 1 |
| Ordinary | H | 300 | 84 – 16 |
| | L | 500 | |
| | LL | 600 | |
| Enstatite | EH | 200 | 82 – 18 |
| | EL | 600 | 87 – 13 |
| Other | K | 600 | – |
| | R | 400 | 92 – 8 |

representation of main belt asteroids and sample parent bodies different from meteorites, or (3) micrometeorites mainly sample cometary bodies (and assumes that comets contain fewer chondrules than asteroids). To differentiate between these possibilities, Genge et al. (2005) and Genge (2006) examined eight coarse-grained and composite (i.e., containing both coarse- and fine-grained components) unmelted micrometeorites, which contained (spherical) igneous objects reminiscent of chondrules based on their textural and geochemical properties. The authors concluded that the fine-grained matrix in composite unmelted micrometeorites was most similar to fine-grained unmelted micrometeorites, previously linked to primitive carbonaceous chondrites such as CI, CR, and CM chondrites (Kurat et al. 1994; Genge et al. 1997; Engrand and Maurette 1998). Hence, at least a fraction of the coarse-grained and composite unmelted micrometeorites contain chondrule fragments and can be directly linked to primitive, chondrule-bearing carbonaceous chondrites, demonstrating their presence in the micrometeorite record.

Recent studies have reached similar conclusions (e.g., Taylor et al. 2008; Van Ginneken et al. 2012; Reshma et al. 2013), while others have argued that JFCs may contribute significantly to the chondrule-bearing micrometeorite population (e.g., Taylor et al. 2012; Suttle et al. 2019a). Dynamical models studying the source bodies of the Zodiacal cloud support a cometary contribution to the micrometeorite source, with possibly up to 85% of the cosmic dust flux to Earth originating from JFCs (Nesvorný et al. 2010). Consequently, micrometeorites appear to sample various types of chondrule-bearing and -free extraterrestrial material that may be (un)known to the meteorite inventory.

Whole or complete chondrules are rare within the micrometeorite record and have only been described in a few instances (e.g., Genge et al. 2005; Genge 2006; Van Ginneken et al. 2012; Suttle et al. 2020; Dionnet et al. 2020). This scarcity can mainly be attributed to the physicochemical properties of chondrules during collisional events and aqueous alteration processes on the parent bodies of micrometeorites, and to the poor preservation potential of chondrules during atmospheric entry heating (see Discussion).

Oxygen isotope ratios may further assist in the identification of micrometeorite precursor bodies and have previously revealed a large discrepancy in the relative contributions from specific meteorite groups (Engrand et al. 2005; Taylor et al. 2005; Yada et al. 2005; Suavet et al. 2010; Cordier et al. 2011, 2012; Cordier and Folco 2014; Van Ginneken et al. 2017; Suttle et al. 2020). For instance, carbonaceous chondrites represent a major component of the micrometeorite population (~60% versus 3% in meteorites), while the abundance of ordinary chondrites is far more limited (~20% versus 72% in meteorites) for particles in the 50–2300 μm size fraction. Shock recovery experiments conducted by Tomeoka et al. (2003) demonstrated that hydrated asteroids are more prone to produce dust particles as a result of explosive decompression in phyllosilicates during shock events. Flynn et al. (2009) confirmed the importance of water in hydrated asteroids during collisional events, but concluded that the preferential breakdown of hydrated asteroids is predominantly determined by their mechanical properties (e.g., friability). Carbonaceous chondrites, including the CM, CI, and CR chondrites, thus appear to produce the highest concentration of small (<300 μm) dust particles. Recently, Genge et al. (2017) demonstrated that the majority of igneous rims in scoriaceous and unmelted micrometeorites contained phyllosilicates prior to atmospheric entry. This would suggest that the explosive decompression of phyllosilicates in the parent asteroids of micrometeorites is negligible and mostly controlled by mechanical disintegration.

Here, we study the Antarctic micrometeorite WF1202A-001, which hosts a unique, complete spherical inclusion, reminiscent of chondrules, that survived both atmospheric entry and subsequent terrestrial alteration. The potential chondrule and surrounding micrometeorite groundmass have been characterized using petrography, geochemistry, and oxygen isotope ratios to constrain the nature of its precursor body. The degree of atmospheric entry heating in micrometeorite WF1202A-001 was estimated and used to constrain its entry parameters and source region within the solar system. This information is used to refine our general understanding of the micrometeorite population in an attempt to identify the variety of parent bodies present within the solar system.

## METHODS

Following the discovery of micrometeorites and -tektites in sedimentary traps from the Transantarctic Mountains (Folco et al. 2008; Rochette et al. 2008), the joint Belgian-Japanese MICROMETA expedition (2012–2013) sampled similar types of sedimentary deposits from a different region on the Antarctic continent, that is, the Sør Rondane Mountains in Drønning Maud Land of East Antarctica (Goderis et al. 2020; Fig. 1). Material was extracted from a series of weathering pits, exposed cracks, and fissured surfaces within a predominant meta-tonalitic host rock (Kojima and Shiraishi 1986; Kamei et al. 2013). The Antarctic environment has proven to be beneficial toward the preservation of meteoritic material due to the (1) cold and dry climate, (2) prolonged accumulation ages (up to several Ma), and (3) absence of anthropogenic contamination. Although weathering conditions vary significantly among the different types of micrometeorite deposits (Van Ginneken et al. 2016), the Sør Rondane Mountain collection appears to be relatively unbiased when compared to other Antarctic collections, including the well-preserved South Pole Water Well collection, and is thus representative of the contemporary cosmic dust flux to Earth (Taylor et al. 2000, 2007; Suavet et al. 2011; Goderis et al. 2020). Based on cosmogenic nuclide dating of granitoid basement rocks from the Walnumfjellet mountain summit, the Sør Rondane Mountains have been deglaciated and exposed to atmospheric fallout, including volcanic ash, microtektites, and cosmic dust, for a time span of ~1–3 Ma (Suganuma et al. 2014), yielding a large, new collection of impact- or extraterrestrial-related materials.
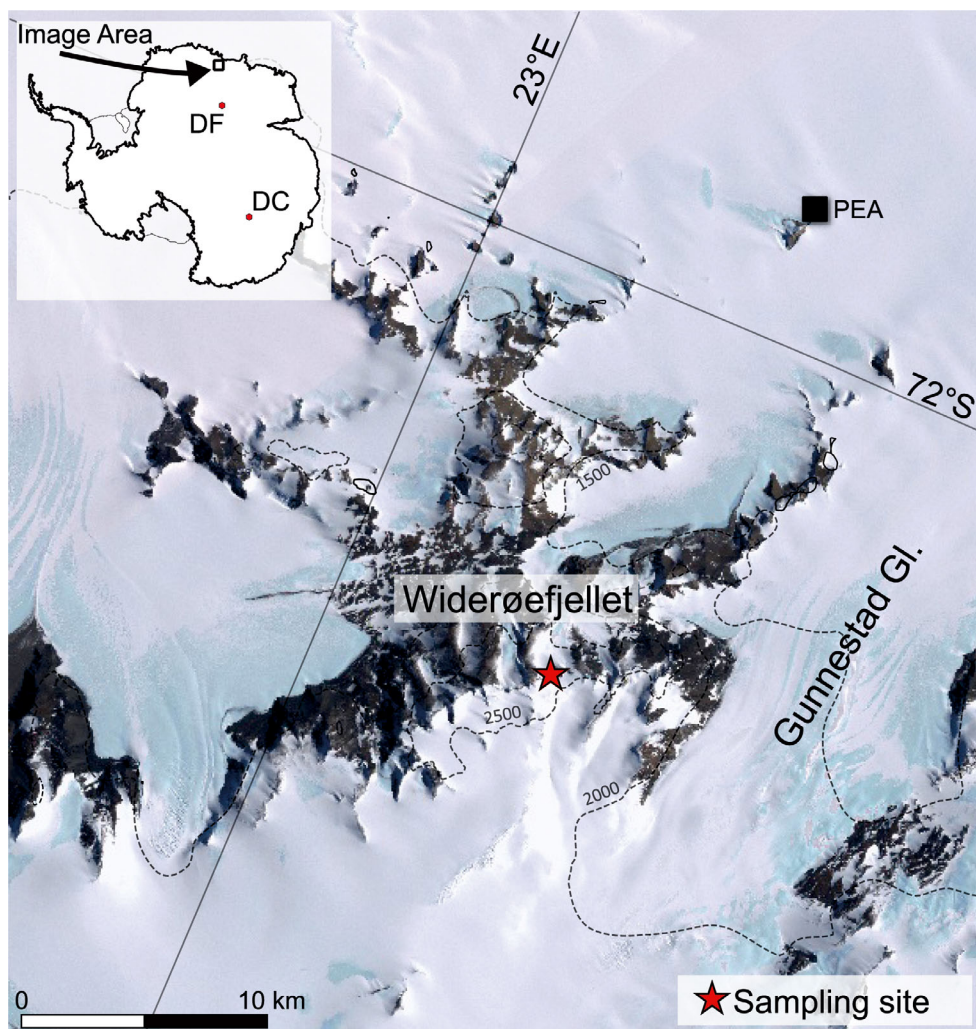
Fig. 1. Detailed map of the Sør Rondane Mountains, indicating the Widerøefjellet sampling site (star symbol) from which micrometeorite WF1202A-001 was extracted. The top left image shows the location of the Sør Rondane Mountains on the Antarctic continent. The abbreviations "DF" and "DC" stand for the Japanese Dome Fuji and French-Italian EPICA Dome C, respectively. (Color figure can be viewed at wileyonlinelibrary.com.)

About 400 g of sedimentary deposits from Widerøefjellet sample site "2A" that was <3000 μm in size was weighed and sieved into six size fractions ranging from <125 μm up to >2000 μm using ultra-pure water to remove the excess of silt and clay particles. The deposit was subsequently placed into a drying oven for approximately 12 h at a constant temperature of ~60°C. The magnetic fraction was extracted from the bulk size fractions using a simple hand magnet. This procedure was repeated until most magnetic particles were extracted. Finally, micrometeorites were handpicked from both the magnetic and nonmagnetic size fractions using a binocular microscope. Particles were imaged using a JEOL JSM IT-300 scanning electron microscope (SEM), coupled to an Oxford energy-dispersive spectrometer (EDS) at the SURF

research unit of the Vrije Universiteit Brussels, Belgium. Following this session, 35 micrometeorites were selected for embedding in epoxy resin based on preliminary SEM-EDS analyses and polished for further analysis. During this stage, we observed the anomalous, spherical inclusion in micrometeorite WF1202A-001, which is characterized and discussed in the current study.

Major and minor elemental compositions were determined using a JEOL JXA-8200 electron probe micro analyzer (EPMA) at the National Institute of Polar Research (Tokyo, Japan) on the embedded and polished micrometeorite WF1202A-001 (Fig. 2). Core-to-rim profiles were acquired for the spherical inclusion (SI), a relict olivine (Ol1), and low-Ca pyroxene grain (Px1), while individual point analyses were performed on metal (M) and sulfide phases (S), and the glassy
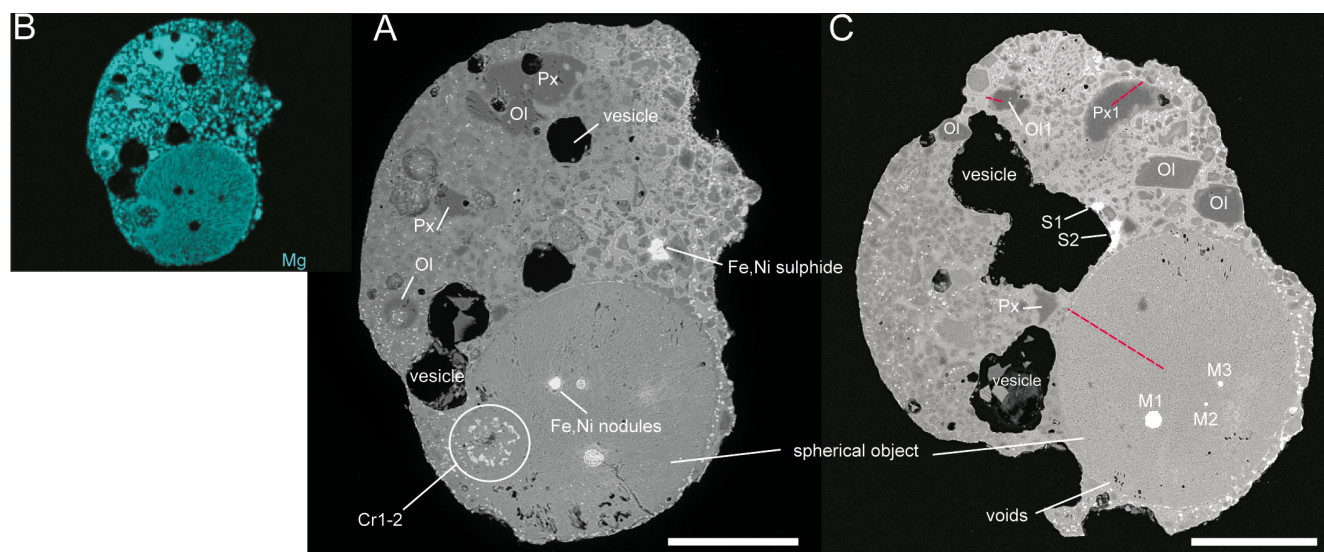
Fig. 2. Sectioned backscatter electron images (BSE) of micrometeorite WF1202A-001, including the spherical inclusion. Large olivine (Ol) and low-Ca pyroxene (Px) grains, and high-density mineral phases including Fe-Ni alloys (M1-3) and sulfides (S1-2) are also present. The left image (A) shows a cluster of chromite/Cr-rich spinel (Cr1-2) grains within the spherical inclusion that surrounds a circular depression. The FeO-rich ($Fo_{63}$) olivine crystals within the spherical inclusion appear to radiate from this particular depression (B). The right image (C) shows the approximate location of EPMA profiles (dashed line) acquired within the spherical inclusion, and a coarse-grained olivine (Ol1) and low-Ca pyroxene (Px1) grain. Scale bar is 100 μm. (Color figure can be viewed at wileyonlinelibrary.com.)

micrometeorite groundmass (GM). All analyses were carried out using a 15 kV accelerating voltage and a focused beam with a diameter of less than 1 μm. The spherical inclusion, relict olivine, and low-Ca pyroxene grain were analyzed using a 30 nA beam current while monitoring the elements Na, Mg, Al, Si, P, Ca, Ti, Cr, Mn, Fe, Ni, and Zn. Sulfide and metal phases were also analyzed using a 30 nA beam current while monitoring Mg, Si, P, S, Cr, Fe, Co, Ni, and Cu. The glassy micrometeorite groundmass was analyzed using a 10 nA beam current while monitoring Na, Mg, Al, Si, P, K, Ca, Ti, Cr, Mn, and Fe. Counting times range from 10 to 100 s on peaks for each mineral. Correction procedures are based on the ZAF method. Natural and synthetic silicates, oxides, and metals with well-known chemical compositions were used as standards (see Haba et al. [2017] for an overview).

The major and trace elemental (57 in total) compositions were also determined using a Teledyne Cetac Technologies Analyte G2 excimer-based laser ablation system coupled to a Thermo Scientific Element XR double-focusing sector field inductively coupled plasma mass spectrometer (LA-ICP-MS) at the Atomic and Mass Spectrometry (A&MS) unit of the Department of Chemistry (Ghent University, Belgium). Two replicate analyses using a beam size of 35 μm were performed on both the spherical inclusion and the groundmass. Additional details regarding the LA-ICP-MS procedures can be found in Das Gupta et al. (2017).

Oxygen isotope ratios were determined using a Cameca IMS 1270 secondary ion mass spectrometer (SIMS) at the Centre de Recherches Pétrographiques et Géochimiques (CRPG – Université de Lorraine, France). The particle was analyzed using a $Cs^+$ ion beam with a spot size of approximately 15 μm and a beam current of ~2.5 nA. Samples were positioned at a physical angle of 10–15° relative to the incoming ion beam. The ions of the three isotopes of oxygen ($^{16}O^-$, $^{17}O^-$, and $^{18}O^-$) were monitored simultaneously in multi-collection mode using Faraday cups. Particles were analyzed for 275 s, pre-sputtering included. Three reference materials—basaltic glass CLDR01, diopside JV1, and Cody Shale SCo1—were analyzed five times at the start and end of each session to compensate for instrumental mass fractionation effects. Based on repeated analysis of the selected reference materials, the analytical uncertainties for the sessions are ± 0.55‰ (2SE) for $\delta^{17}O$, ~±0.53‰ (2SE) for $\delta^{18}O$, and ~±0.62‰ (2SE) for $\Delta^{17}O$, where SE is the standard error calculated based on a total of 61 sample analyses.

## RESULTS

### Petrography

Particle WF1202A-001 is a 394x358 μm, silicate-dominated (S-type) cosmic spherule with a micro-porphyritic texture, following the classification system

of Genge et al. (2008; Fig. 2). This micrometeorite has an asymmetric shape with a smooth rounded margin along most of the particle exterior. This surface is truncated by a subangular, irregular-shaped edge along one side (Fig. 2A,B). As observed in a deeper section (Fig. 2C), the irregular shape arises from the partial detachment of a portion of the micrometeorite, which is almost completely separated from the main mass as the result of a chain of vesicles up to 150 μm in diameter.

The internal mineralogy of micrometeorite WF1202A-001 is composed primarily of <10 μm olivine micro-phenocrysts ($Fo_{80-84}$) and magnetite crystallites suspended within a glassy, Si-Fe-Al-Ca-enriched groundmass. However, several larger (>30 μm) anhydrous silicates are also present. They have strongly Mg-enriched compositions, angular morphologies, and are cut across by internal fractures (Fig. 3). These Mg-rich silicates include both olivine ($Fo_{98-99}$) and low-Ca pyroxene ($En_{98-99}$, $Wo_{0-1}$) grains—the former display normally zoned profiles, while the latter are overgrown by an FeO-rich ($Fo_{66}$) olivine mantle. Accessory high-density mineral phases (up to several tens of micrometer in size) are identified as Fe-Ni sulfides. Within the micrometeorite, a large spherical inclusion with an apparent average diameter of ~209 μm (220 × 197 μm, ellipticity: ε = 1.12—determined from Fig. 2C), as observed in 2-D section view (the maximum diameter is likely slightly larger), is present. The spherical inclusion has a milky white color when viewed with a binocular microscope. The boundary between the host particle and the spherical inclusion is represented by a sharp, well-defined contact, while the micrometeorite's local groundmass adjacent to the inclusion contains tens of micron-sized olivine and oxide mineral phases (Fig. 4). In contrast to the groundmass, the spherical inclusion is primarily composed of FeO-rich olivine ($Fo_{66}$) crystals up to 10 μm in diameter arranged in a barred olivine texture and embedded in a mesostasis glass, predominantly composed of Si, Fe, Ca, and Al. The fayalitic olivine is characterized by subtle profiles displaying normal zoning and radiate outward from a circular region within the spherical inclusion. This region contains tens of small (up to 10 μm) Cr-rich spinel grains (Fig. 2B; Table 2). Small, rounded Fe-Ni metal grains are also observed within the spherical inclusion and reach up to 10 μm in size. In addition, a series of circular/elliptical voids and microscopic oxide grains, presumably consisting of magnetite, appear to be present along the inclusion's margin (Fig. 2C).

## Geochemistry

The groundmass is characterized by a highly variable major elemental composition, reflecting
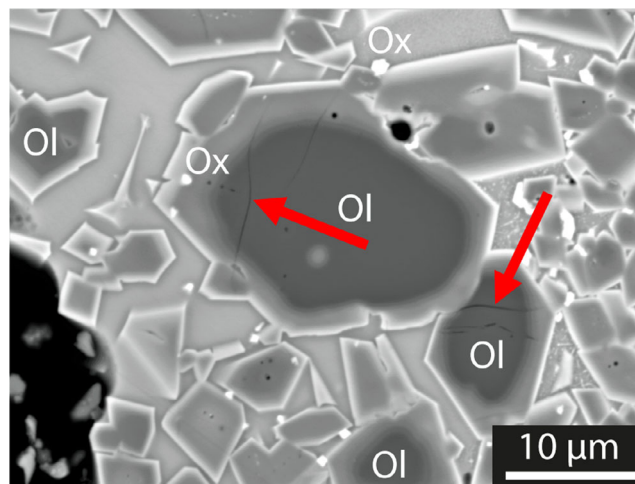


Fig. 3. Backscatter electron images of internal fractures (arrows) in relict olivine crystals. The latter can be distinguished from neo-formed crystals due to their higher MgO content (characterized by their low Z-contrast in BSE) and anhedral, subrounded shapes. Abbreviations: Ol—olivine, Ox—oxide. (Color figure can be viewed at wileyonlinelibrary.com.)

different proportions of glassy mesostasis (e.g., $Al_2O_3$ ~7–10 wt%, FeO ~19–29 wt%, MgO ~2–12 wt%, $SiO_2$ ~47–53 wt%) and olivine micro-phenocrysts (e.g., $Al_2O_3$ ~0.78 wt%, FeO ~15 wt%, MgO ~41 wt%, $SiO_2$ ~42 wt%), captured in each broad-beam analysis. The EPMA spot analysis mainly sampled the glassy mesostasis, which is predominantly composed of Si, Al, Fe, and Ca, and depleted in Mg compared to the olivine micro-phenocrysts (Table 3). In contrast, the larger LA-ICP-MS spot analyses sampled a mixture of both components and indicate an overall chondritic signature for the major elemental components (within a factor of 0.5–1.4 times CI chondrite), except for Na and K (Fig. 5; Table 3 and 4). The REE pattern is broadly flat with respect to CI chondrite values (Fig. 6; McDonough and Sun 1995). In an Fe/Mg versus Fe/Mn diagram (Fig. 7A), the micrometeorite groundmass plots at the edge of the chondritic field. The Mg/Al versus Si/Al ratios support the chondritic nature of the micrometeorite groundmass, displaying similar compositions as the groundmass observed in CM, CI, and CV chondrites (Fig. 7B).

A series of EPMA line transects were conducted on the larger phases within particle WF1202A-001. These include one of the relict MgO-rich olivines (Ol1—Fig. 8) and pyroxene grains (Px1—Fig. 9), as well as the spherical inclusion (Fig. 10). The bulk EPMA data of the spherical inclusion are summarized in Fig. 11. Magnesium-rich olivine grain Ol1 has a core composition (represented by position O1–O10 in Fig. 8, see Data S1 in supporting information) averaging an Mg# of 98 (Mg#=Mg/[Mg + Fe]*100, in at%). This
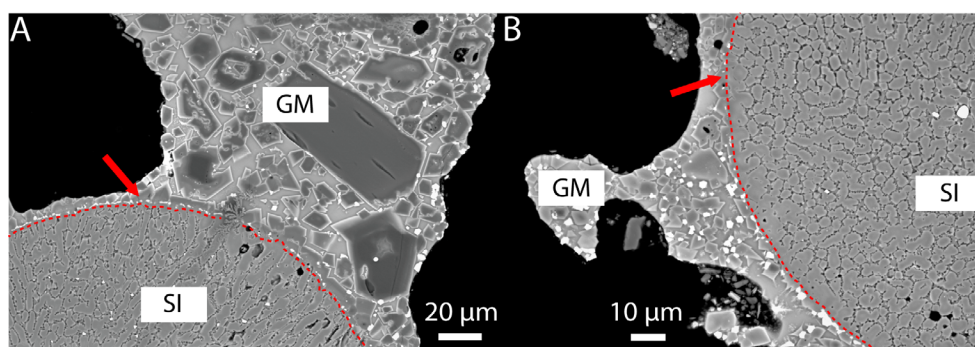
Fig. 4. Backscatter electron images of the transition (dashed line) between the spherical inclusion and the groundmass (arrows). The transition is sharp, with neo-formed olivine and magnetite crystals nucleating at the rim of the chondrule. (Color figure can be viewed at wileyonlinelibrary.com.)

Table 2. Major and minor elemental concentrations (wt%) of Cr-rich spinel/chromite phases in the spherical inclusion (see Fig. 2A) determined with SEM-EDS.

| Analysis no. | Fe | O | Cr | Mg | Al | Si | Mn | Ca | Ti | Ni | V | Total |
|---|---|---|---|---|---|---|---|---|---|---|---|---|
| Cr1 | 33.7 | 31.5 | 18.8 | 6.0 | 5.0 | 3.8 | 0.5 | 0.2 | 0.2 | 0.2 | 0.1 | 100 |
| Cr2 | 36.1 | 31.4 | 16.0 | 7.1 | 3.3 | 4.9 | 0.4 | 0.3 | 0.2 | 0.2 | n.d. | 99.9 |

Table 3. Major and minor elemental oxide abundances (wt%) in the micrometeorite groundmass according to individual EPMA spot analyses. No average compositions were calculated due to the highly heterogeneous nature of the groundmass, consisting of olivine phenocrysts, magnetite, and glassy mesostasis. The heterogeneity observed can be attributed to the local occurrence of different proportions of the aforementioned components.

| Analysis no. | $Na_2O$ | $Al_2O_3$ | $K_2O$ | $FeO^a$ | $TiO_2$ | MnO | MgO | $SiO_2$ | $Cr_2O_3$ | CaO | NiO | $P_2O_5$ | Total |
|---|---|---|---|---|---|---|---|---|---|---|---|---|---|
| Limit of detection (LOD) | 0.007 | 0.01 | 0.01 | 0.01 | 0.04 | 0.03 | 0.01 | 0.02 | 0.02 | 0.01 | 0.04 | 0.02 | |
| GM1 | 0.11 | 8.82 | <LOD | 23.8 | 0.41 | 0.72 | 4.16 | 51.3 | 0.08 | 8.00 | <LOD | 0.36 | 97.7 |
| GM2 | <LOD | 0.78 | <LOD | 15.3 | 0.04 | 0.35 | 40.7 | 41.6 | 0.20 | 0.69 | 0.15 | 0.28 | 100.1 |
| GM3 | 0.12 | 9.75 | 0.02 | 28.6 | 0.43 | 0.55 | 2.35 | 48.1 | 0.22 | 7.91 | <LOD | 0.46 | 98.5 |
| GM4 | <LOD | 8.76 | <LOD | 28.2 | 0.26 | 0.54 | 2.72 | 47.0 | 0.04 | 9.67 | <LOD | 0.66 | 97.8 |
| GM5 | 0.23 | 7.56 | 0.02 | 18.9 | 0.34 | 0.71 | 11.9 | 52.3 | 0.05 | 6.49 | <LOD | 0.40 | 99.0 |

[a]All iron expressed as FeO.

value progressively decreases through the rim toward a final FeO-rich composition with an Mg# of 58. The core displays low $Cr_2O_3$ (0.31–0.39 wt%), CaO (0.19–0.33 wt%), ZnO (<0.04 wt%—not shown in Fig. 8) and $TiO_2$ (<0.02–0.04 wt%—not shown in Fig. 8) contents. In contrast, the rim shows a corresponding increase in MnO (0.05–0.35 wt%), NiO (0.05–0.30 wt%), and $P_2O_5$ (0.02–0.16 wt%) contents concurrent with the higher FeO concentrations.

A similar profile is observed for the large relict low-Ca pyroxene crystal (Px1; Fig. 2C), for which the core (P1–P10, Fig. 9 and see Data S2 in supporting information) concurs with the Mg endmember, with an Mg# of ~99 and minimal $Al_2O_3$ (<0.04 wt%), MnO (<0.07 wt%), $P_2O_5$ (<0.03 wt%—not shown in Fig. 9), CaO (<0.05 wt%), $TiO_2$ (<0.02 wt%—not shown in

Fig. 9), and NiO (<0.05 wt%) contents, but with a markedly higher $Cr_2O_3$ level (0.56–0.80 wt%). A sharp change in $SiO_2$ content marks a sudden transition from the core to the rim of the grain (P11–P15) and corresponds to an overgrowth by FeO-rich olivine ($Fo_{66}$). The $Na_2O$ concentrations (not shown in Fig. 9) progressively decrease from the core to rim following a linear trend that is distinct from what is observed for all other elements.

The spherical inclusion has a heterogeneous major and minor elemental composition, with significant geochemical variations on a micrometer-length scale (Fig. 10). Within the inclusion, the $Cr_2O_3$ concentration is relatively constant at an average of 0.45 wt% and increases only at the rim to a value of ≃16.4 wt%, presumably related to the presence of Cr-rich spinel
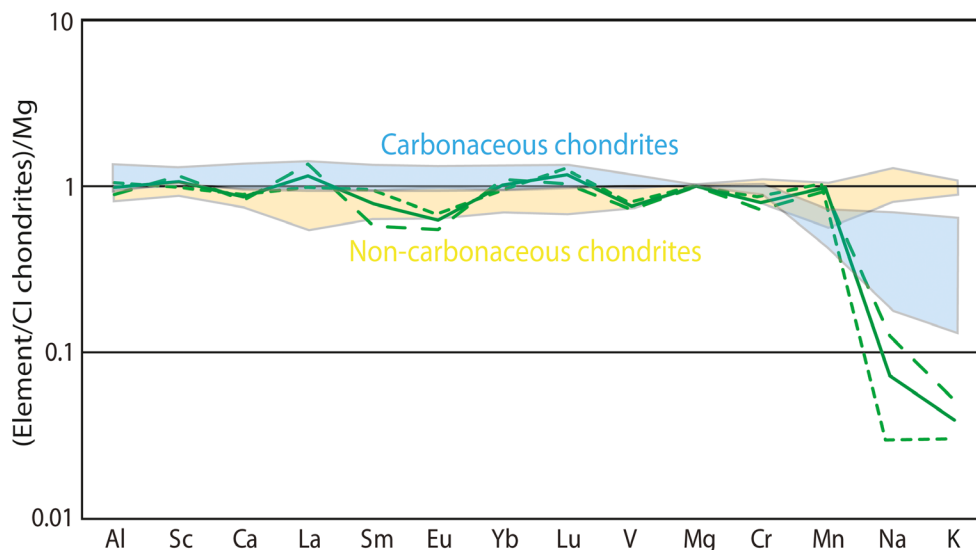
Fig. 5. Major and minor lithophile elemental pattern determined by LA-ICP-MS and normalized to CI chondrites (McDonough and Sun 1995) and Mg. The dashed lines represent individual measurements acquired on the micrometeorite groundmass, while the full line represents the mean value of both. While the micrometeorite groundmass is overall chondritic, it does not appear to match a specific chondrite group, positioned within the compositional ranges observed for both carbonaceous and noncarbonaceous chondrites, with the exception of the volatile elements Na and K. Reference values for carbonaceous and non-carbonaceous chondrites used are from Kallemeyn and Wasson (1981, 1982, 1985) and Kallemeyn et al. (1978, 1989, 1991, 1994, 1996). (Color figure can be viewed at wileyonlinelibrary.com.)

phases. Less marked enrichments at the inclusion's rim are also observed for $TiO_2$ (0.45 wt%—not shown in Fig. 10), $Al_2O_3$ (6.96 wt%), and NiO (0.17 wt%), although the concentrations of these elements display minor variation within the core of the inclusion only (<0.02–0.16 wt%, 0.05–2.92 wt%, and <0.04–0.06 wt%, respectively). By contrast, $SiO_2$ exhibits a large compositional range (37.8–50.5 wt%), locally increasing up to ~50 wt%, but decreasing to ~25 wt% at the inclusion rim. Similarly, the FeO, MgO, and CaO contents display smaller to moderately large compositional ranges (~26–30 wt%, ~15–35 wt%, ~0.10–3 wt%, respectively) and display no clear spatial relationship between the core and rim. In contrast, their variations correspond to differences in the proportion of crystals and matrix, as demonstrated by local correlated enrichments in $Na_2O$, $Al_2O_3$, $TiO_2$, $SiO_2$, and $P_2O_5$ (primarily in the glass phase) and corresponding depletions in FeO and MgO (primarily in the olivine phenocrysts).

A representative bulk composition was determined by averaging the line transect data (analyses SI1–SI14 in Data S3—see supporting information). This bulk composition falls close to the range reported for type II porphyritic chondrules within the primitive ordinary chondrite LL3.00 Semarkona (Jones 1990), although deviations are observed for Mn and the moderately volatile elements Na and K (Fig. 11). In a Fe/Mg versus. Fe/Mn diagram (Fig. 7A), the spherical inclusion plots around the 4-Vesta reference line, indicating a non-chondritic composition. This is confirmed by the Mg/Al versus Si/Al diagram (Fig. 7B), where the spherical inclusion plots at considerably higher Mg/Al and Si/Al ratios, demonstrating the Al-poor nature of this component. The bulk spherical inclusion shows a broadly flat subchondritic REE pattern (with respect to CI chondrite data). As mentioned above, the spherical inclusion also contains several high-density Fe-Ni-rich phases. These phases generally lack lithophile elements or sulfur (see Data S4 in supporting information) and hence represent Fe-Ni metal. The Fe/Ni ratio within these grains varies from 6.87 in the largest grain to less than 0.19 in the smaller nodules. These lower Fe/Ni ratios correspond to relatively high concentrations of Si, suggesting that at least some of these analyses are affected by beam overlap with the surrounding silicate phases. Stoichiometric considerations based on EPMA data infer the presence of high-Ni kamacite or taenite, and possibly awaruite ($Ni_2Fe$ to $Ni_3Fe$). The latter phase was previously identified in chondrules from the CV3 Allende meteorite (Rubin 1991). High-density Fe-rich phases are also found within the micrometeorite groundmass, but these contain both Ni and S. Consequently, they are interpreted as sulfides. Based on EPMA data, the sulfides most likely represent

Table 4. Individual and average major (wt%) and trace (µg/g) element concentrations resulting from LA-ICP-MS analyses of the spherical inclusion (SI) and micrometeorite groundmass (GM).

| Element | SI-1 | SI-2 | SI-avg. | GM-1 | GM-2 | GM-avg. | LOD |
|---|---|---|---|---|---|---|---|
| Li (µg g$^{-1}$) | <LOD | <LOD | <LOD | <LOD | 11.9 | 11.9 | 7 |
| Be (µg g$^{-1}$) | <LOD | <LOD | <LOD | 0.35 | <LOD | 0.35 | 0.1 |
| Na$_2$O (wt%) | 0.031 | 0.027 | 0.029 | 0.11 | 0.032 | 0.073 | 0.002 |
| MgO (wt%) | 23.7 | 24.9 | 24.3 | 21.0 | 25.8 | 23.4 | 0.0004 |
| Al$_2$O$_3$ (wt%) | 0.67 | 0.73 | 0.70 | 1.89 | 2.75 | 2.32 | 0.0002 |
| SiO$_2$ (wt%) | 45.4 | 44.2 | 44.8 | 44.2 | 40.0 | 42.1 | 0.009 |
| P$_2$O$_5$ (wt%) | 0.13 | 0.16 | 0.15 | 0.27 | 0.36 | 0.32 | 0.002 |
| S (µg g$^{-1}$) | 2.38 | 2.19 | 2.28 | 3.39 | 3.44 | 3.41 | 0.02 |
| K$_2$O (wt%) | <LOD | <LOD | <LOD | 0.0044 | 0.0031 | 0.0038 | 0.0003 |
| CaO (wt%) | 0.78 | 0.83 | 0.80 | 1.38 | 1.85 | 1.61 | 0.004 |
| Sc (µg g$^{-1}$) | 3.72 | 3.56 | 3.64 | 9.03 | 9.39 | 9.21 | 0.06 |
| TiO$_2$ (wt%) | 0.035 | 0.032 | 0.033 | 0.065 | 0.092 | 0.079 | 0.004 |
| V (µg g$^{-1}$) | 60 | 59.3 | 59.6 | 52.57 | 72.0 | 62.3 | 0.09 |
| Cr (µg g$^{-1}$) | 3842 | 2877 | 3360 | 2489 | 3668 | 3078 | 0.4 |
| MnO (wt%) | 0.90 | 0.71 | 0.81 | 0.30 | 0.41 | 0.36 | 0.00002 |
| FeO* (wt%) | 27.9 | 27.6 | 27.7 | 30.4 | 28.3 | 29.3 | 0.0007 |
| Co (µg g$^{-1}$) | 74.5 | 200 | 137 | 675 | 200 | 438 | 0.2 |
| Ni (µg g$^{-1}$) | 1128 | 5434 | 3281 | 1567 | 980 | 1273 | 1 |
| Cu (µg g$^{-1}$) | <LOD | 0.66 | 0.66 | 2.06 | 2.38 | 2.22 | 0.1 |
| Zn (µg g$^{-1}$) | <LOD | 1.58 | 1.58 | 2.81 | 0.20 | 1.50 | 0.5 |
| Ga (µg g$^{-1}$) | 0.066 | 0.17 | 0.12 | 1.13 | 1.12 | 1.13 | 0.06 |
| Ge (µg g$^{-1}$) | <LOD | 0.20 | 0.20 | <LOD | <LOD | <LOD | 0.06 |
| As (µg g$^{-1}$) | <LOD | 0.19 | 0.19 | <LOD | 0.23 | 0.23 | 0.05 |
| Rb (µg g$^{-1}$) | 0.071 | 0.11 | 0.092 | 0.042 | 0.14 | 0.090 | 0.03 |
| Sr (µg g$^{-1}$) | 4.79 | 4.21 | 4.50 | 9.13 | 11.8 | 10.5 | 0.1 |
| Y (µg g$^{-1}$) | 0.78 | 0.85 | 0.82 | 2.24 | 2.44 | 2.34 | 0.01 |
| Zr (µg g$^{-1}$) | 2.13 | 1.74 | 1.93 | 5.04 | 5.43 | 5.24 | 0.02 |
| Nb (µg g$^{-1}$) | 0.13 | 0.23 | 0.18 | 0.37 | 0.46 | 0.42 | 0.004 |
| Mo (µg g$^{-1}$) | 0.17 | 0.14 | 0.15 | 1.17 | 0.40 | 0.79 | 0.1 |
| Sn (µg g$^{-1}$) | <LOD | 0.17 | 0.17 | 0.10 | <LOD | 0.10 | 0.04 |
| Sb (µg g$^{-1}$) | 0.14 | <LOD | 0.14 | 0.24 | <LOD | 0.24 | 0.01 |
| Cs (µg g$^{-1}$) | 0.018 | <LOD | 0.018 | 0.014 | 0.018 | 0.016 | 0.008 |
| Ba (µg g$^{-1}$) | 1.21 | 1.61 | 1.41 | 3.53 | 4.44 | 3.99 | 0.1 |
| La (µg g$^{-1}$) | 0.13 | 0.13 | 0.13 | 0.42 | 0.37 | 0.40 | 0.008 |
| Ce (µg g$^{-1}$) | 0.47 | 0.50 | 0.48 | 0.87 | 1.10 | 0.99 | 0.0007 |
| Pr (µg g$^{-1}$) | 0.086 | 0.023 | 0.054 | 0.15 | 0.11 | 0.13 | 0.0001 |
| Nd (µg g$^{-1}$) | 0.16 | 0.67 | 0.42 | 0.73 | 1.04 | 0.89 | 0.002 |
| Sm (µg g$^{-1}$) | 0.053 | <LOD | 0.053 | 0.11 | 0.23 | 0.17 | 0.0008 |
| Eu (µg g$^{-1}$) | <LOD | 0.035 | 0.035 | 0.040 | 0.061 | 0.051 | 0.02 |
| Gd (µg g$^{-1}$) | 0.22 | 0.19 | 0.21 | 0.26 | 0.29 | 0.28 | 0.03 |
| Tb (µg g$^{-1}$) | 0.037 | <LOD | 0.037 | 0.057 | 0.059 | 0.058 | 0.004 |
| Dy (µg g$^{-1}$) | 0.11 | 0.18 | 0.14 | 0.30 | 0.42 | 0.36 | 0.01 |
| Ho (µg g$^{-1}$) | 0.038 | 0.021 | 0.030 | 0.098 | 0.083 | 0.091 | 0.004 |
| Er (µg g$^{-1}$) | 0.13 | 0.14 | 0.14 | 0.25 | 0.31 | 0.28 | 0.01 |
| Tm (µg g$^{-1}$) | 0.025 | 0.016 | 0.021 | 0.040 | 0.033 | 0.037 | 0.0001 |
| Yb (µg g$^{-1}$) | 0.097 | 0.0057 | 0.051 | 0.23 | 0.24 | 0.24 | 0.0004 |
| Lu (µg g$^{-1}$) | 0.016 | 0.013 | 0.015 | 0.033 | 0.051 | 0.042 | 0.0001 |
| Hf (µg g$^{-1}$) | <LOD | 0.031 | 0.031 | 0.13 | 0.22 | 0.18 | 0.0002 |
| Ta (µg g$^{-1}$) | 0.016 | 0.017 | 0.017 | 0.0042 | 0.021 | 0.013 | 0.0001 |
| W (µg g$^{-1}$) | 0.079 | 0.072 | 0.075 | 0.038 | 0.23 | 0.14 | 0.0003 |
| Re (µg g$^{-1}$) | <LOD | 0.014 | 0.014 | <LOD | <LOD | <LOD | 0.0007 |
| Ir (µg g$^{-1}$) | <LOD | 0.15 | 0.15 | 0.059 | 0.081 | 0.070 | 0.0004 |
| Pt (µg g$^{-1}$) | 0.081 | 0.28 | 0.18 | 0.15 | 0.12 | 0.13 | 0.0006 |

Table 4. *Continued.* Individual and average major (wt%) and trace (µg/g) element concentrations resulting from LA-ICP-MS analyses of the spherical inclusion (SI) and micrometeorite groundmass (GM).

| Element | SI-1 | SI-2 | SI-avg. | GM-1 | GM-2 | GM-avg. | LOD |
|---|---|---|---|---|---|---|---|
| Hg (µg g$^{-1}$) | <LOD | 0.45 | 0.45 | <LOD | 0.039 | 0.039 | 0.08 |
| Pb (µg g$^{-1}$) | 0.079 | <LOD | 0.079 | 0.090 | 0.092 | 0.091 | 0.0002 |
| Th (µg g$^{-1}$) | <LOD | <LOD | <LOD | 0.048 | 0.075 | 0.061 | 0.00003 |
| U (µg g$^{-1}$) | 0.038 | 0.010 | 0.024 | 0.16 | 0.033 | 0.095 | 0.00004 |

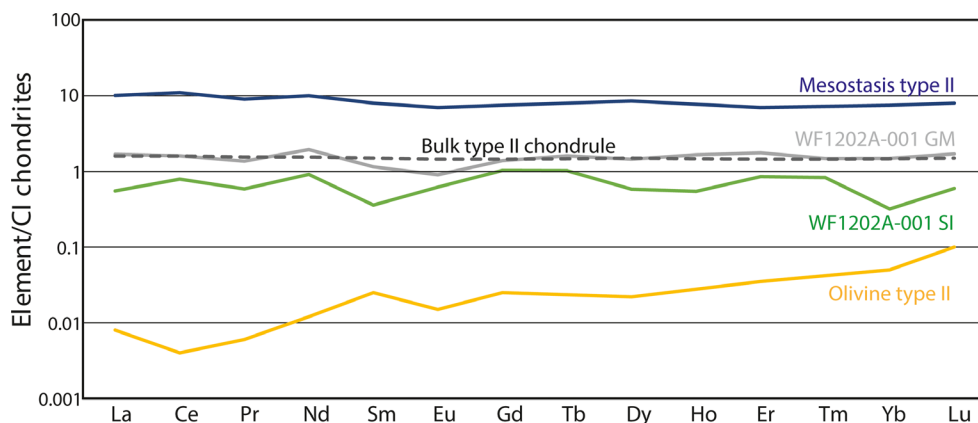Abbreviation: LOD = limit of detection.
[a]All iron expressed as FeO.



Fig. 6. Average rare earth element (REE) concentrations of the spherical inclusion and micrometeorite groundmass normalized to CI chondrites (McDonough and Sun 1995). The spherical inclusion is mostly characterized by subchondritic REE concentrations, except for Gd and Tb. The micrometeorite groundmass is mostly characterized by suprachondritic REE concentrations and displays a relatively flat pattern, very similar to the REE pattern modeled for type II chondrules from ordinary chondrites. Reference data for bulk type II chondrules and their components reproduced from Jacquet et al. (2015). (Color figure can be viewed at wileyonlinelibrary.com.)

pentlandite $(Fe_{0.66}Ni_{0.34})_9S_8$ and monosulfide solutions $(Fe_{0.92}Ni_{0.08})S$. The presence of these sulfide phases suggests that the terrestrial residence time of the particle was relatively short, and/or that weathering remained limited (Van Ginneken et al. 2016).

**Oxygen Isotope Ratios**

Triple-oxygen isotope data were collected for the main components of the particle, that is, the groundmass; a relict olivine grain (Ol1); a large, low-Ca pyroxene grain (Px1); and the spherical inclusion (Figs. 12–14 and see Data S5 in supporting information). The micrometeorite groundmass is characterized by an average $\delta^{17}O$ of 3.46‰, $\delta^{18}O$ of 10.43‰, and $\Delta^{17}O$ of –1.96‰ ($n = 3$). These values plot within the CM carbonaceous chondrite field (Fig. 12), at the higher end of the $\delta^{18}O$ values for this meteorite group.

The relict olivine grain measured is characterized by an extremely $^{16}O$-rich composition with a $\delta^{17}O$ of –45.8‰, $\delta^{18}O$ of –43.7‰, and $\Delta^{17}O$ of –23.1‰ ($n = 1$). This isotopic composition plots between the

carbonaceous chondrite anhydrous mineral (CCAM with a slope of $0.94 \pm 0.01$ (2SE) and intercept of –0.94; Clayton and Mayeda 1999) and Young & Russell (Y&R; Young and Russell 1998) lines (Fig. 13), toward solar compositions ($\delta^{17}O$ of –59.1‰, $\delta^{18}O$ of –58.5‰; Clayton et al. 1977; McKeegan et al. 2011). The Y&R line represents a slope ~ 1 line defined by the oxygen isotopic composition of CAIs extracted from the CV3 Allende meteorite.

In contrast, the large, low-Ca pyroxene grain plots along the Y&R line but at significantly more $^{18}O$-rich (heavy) compositions with a $\delta^{17}O$ of –4.96‰, $\delta^{18}O$ of –4.32‰, and $\Delta^{17}O$ of –2.71‰ ($n = 1$). This is close to the intersection between the Y&R line and the terrestrial fractionation line (TFL = $\delta^{17}O$ – $0.52 \times \delta^{18}O$; Clayton 1993). Both the values of the relict olivine and pyroxene are consistent with refractory minerals commonly observed in CAIs and This abbreviation was removed in earlier versions of the text. AOAs can thus be changed to 'amoeboid olivine aggregates'

Finally, the spherical inclusion has an average $\delta^{17}O$ of –0.98‰, $\delta^{18}O$ of –2.16‰, and $\Delta^{17}O$ of 0.15‰ ($n = 3$).
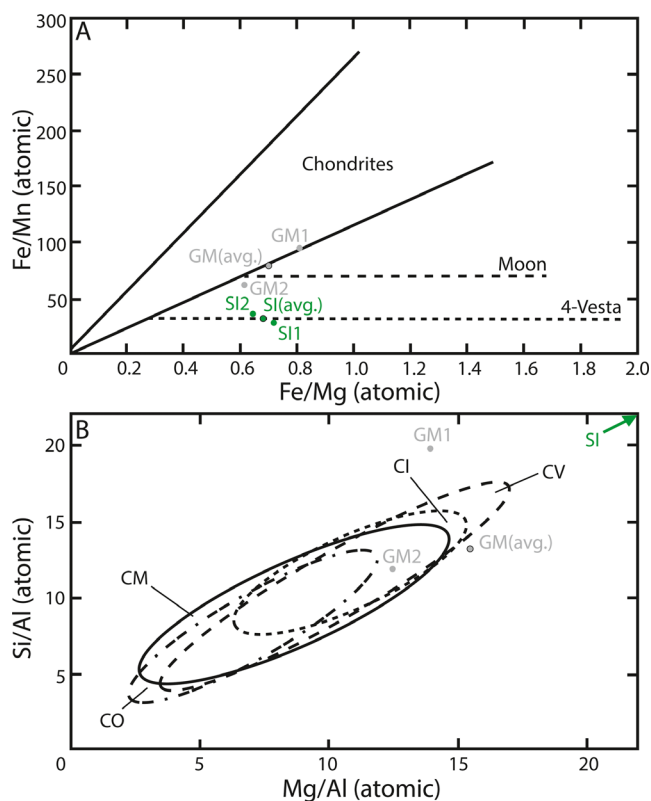
Fig. 7. Major elemental composition of the micrometeorite WF1202A-001 groundmass (GM) and spherical inclusion (SI) plotted in Fe/Mg versus Fe/Mn (A) and Si/Al versus Mg/Al (B) diagrams. The micrometeorite groundmass is positioned along the edge of the chondritic compositional field in (A) and appears to display a similar compositional range as observed in the matrix of CM, CI, and CV chondrites (B). The spherical inclusion plots along the 4-Vesta reference line and does not appear to be chondritic in composition (A). Its composition also appears to be extremely depleted in Al, as demonstrated in (B). Reference values for (A) reproduced from Goodrich and Delaney (2000), and (B) from McSween and Richardson (1977), McSween (1987), and Zolensky et al. (1993). (Color figure can be viewed at wileyonlinelibrary.com.)

The oxygen isotopic data of the spherical inclusion are thus positioned close to the TFL, left of the enstatite chondrite field at significantly lower $\delta^{18}O$ values (Figs. 12 and 14). This isotopic composition does not match any previously reported data for chondrules or bulk chondrites and is therefore considered anomalous.

## DISCUSSION

### The Extraterrestrial Nature of Micrometeorite WF1202A-001: Clues from Petrography and Geochemistry

To distinguish microscopic extraterrestrial particles from their terrestrial counterparts, Genge et al. (2008) have defined a number of criteria that are characteristic
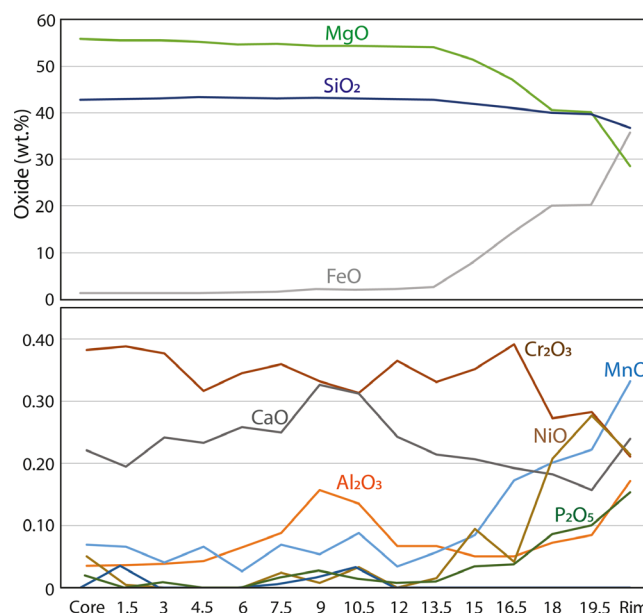


Fig. 8. Major (top) and minor (bottom) elemental oxide concentrations (wt%) determined by EPMA along a core–rim transect in a coarse-grained, relict olivine crystal (Ol1—Fig. 2C). The first and last analyses within the transect are referred to as "Core" and "Rim." The distance of intermediate analyses was measured from the start of the transect and is displayed on the X-axis. (Color figure can be viewed at wile yonlinelibrary.com.)

of micrometeorites (1) the presence of a partial or complete magnetite rim, that developed during atmospheric entry (Toppani et al. 2001; Toppani and Libourel 2003); (2) the presence of Fe-Ni metal; and This should be 3) a bulk chondritic composition, provided crystal sizes are considerably smaller than the overall particle size. These features have been observed in micrometeorite WF1202A-001 and we can thus confirm the extraterrestrial nature of this particle (see Figs. 2 and 5–6).

The texture of micrometeorite WF1202A-001 is consistent with porphyritic S-type cosmic spherules, implying high degrees of melting (>50%; Genge et al. 2008) during atmospheric entry with peak temperatures above the solidus of the chondritic matrix (>1400°C; Toppani et al. 2001). Consequently, the pre-atmospheric textural and geochemical properties of such cosmic spherules may potentially have been (severely) modified. A large fraction of the groundmass of WF1202A-001 has recrystallized, producing neo-formed FeO-rich (Fo$_{80-84}$) olivine, olivine overgrowth rims, and magnetite embedded in a glassy mesostasis, consistent with quench-cooling during atmospheric entry. Nevertheless, the geochemistry of the groundmass remains broadly chondritic, except for significant depletions in Na and K (Figs. 5 and 6). These moderately volatile elements with
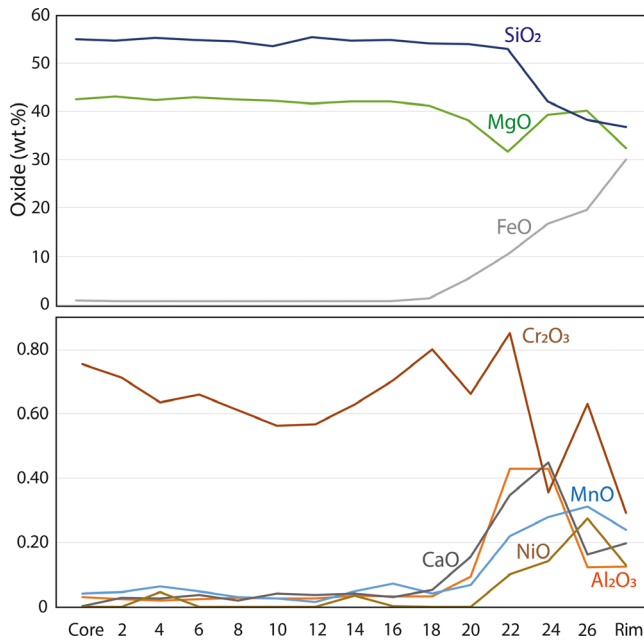
Fig. 9. Major (top) and minor (bottom) elemental oxide concentrations (wt%) determined by EPMA along a core–rim transect in a coarse-grained, relict low-Ca pyroxene (Px1—Fig. 2C) crystal. The first and last analyses within the transect are referred to as "Core" and "Rim." The distance of intermediate analyses was measured from the start of the transect and is displayed on the X-axis. (Color figure can be viewed at wileyonlinelibrary.com.)
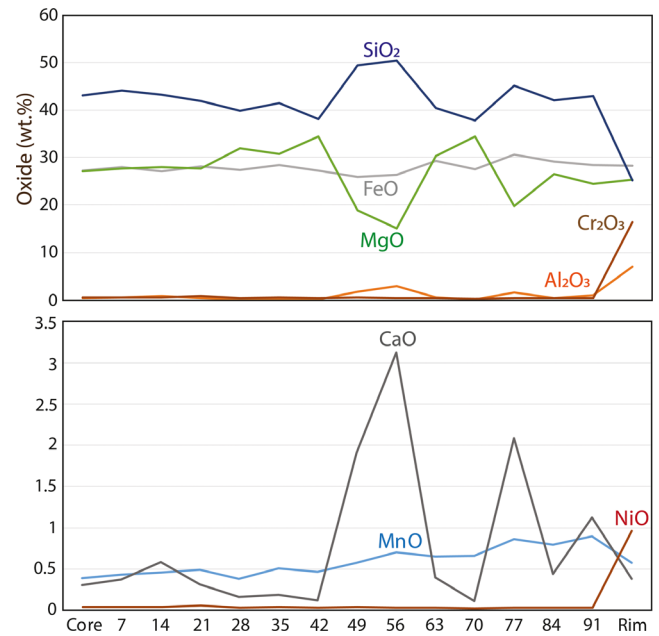


Fig. 10. Major (top) and minor (bottom) elemental oxide concentrations (wt%) determined by EPMA along a core–rim transect in the spherical inclusion (SI—Fig. 2C). The first and last analyses within the transect are referred to as "Core" and "Rim." The distance of intermediate analyses was measured from the start of the transect and is displayed on the X-axis. (Color figure can be viewed at wileyonlinelibrary.com.)

50% condensation temperatures of 958 and 1006K (Lodders 2003), respectively, are strongly evaporated as a result of atmospheric entry heating. The chondritic nature of micrometeorite WF1202A-001 is further supported by its Fe/Mg versus Fe/Mn relations (Fig. 7A; Goodrich and Delaney 2000; Taylor et al. 2007) and suggests a possible affiliation with matrix compositions from CI, CM, or CV chondrites based on its distribution in Mg/Al versus Si/Al space (Fig. 7B; McSween and Richardson 1977; McSween 1987; Zolensky et al. 1993; Taylor et al. 2005). Since CI chondrites do not contain chondrules as a result of intense aqueous alteration, a CM or CV chondrite parent body appears more plausible. These results thus imply that the geochemical composition of the original dust particle was largely preserved despite atmospheric entry heating.

Within the micrometeorite groundmass, some of the olivine (micro-)phenocrysts have anhedral, irregular-shaped cores with diffuse boundaries that gradually transition into the FeO-rich (Fo$_{65}$) rims. These are characteristic features of relict olivine phases in micrometeorites (Genge et al. 2016) and represent ~5–10% of the micrometeorite's surface area (Fig. 2). Their
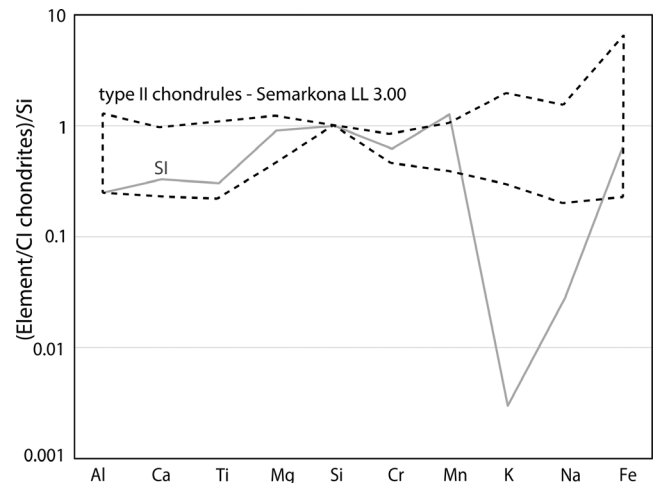


Fig. 11. Major elemental concentrations (wt%) of the spherical inclusion (SI) and comparison with type II porphyritic chondrules from the LL3.00 Semarkona chondrite (Jones 1990). Elemental abundances have been normalized to CI chondrites (McDonough and Sun 1995) and Si. The spherical inclusion is largely positioned within the elemental range determined for Semarkona type II chondrules, except in the case of Mn, K, and Na.

composition is also highly refractory with Mg# between 98 and 99 (Fig. 8 and see Data S1), typically observed in carbonaceous chondrites and their CAIs.
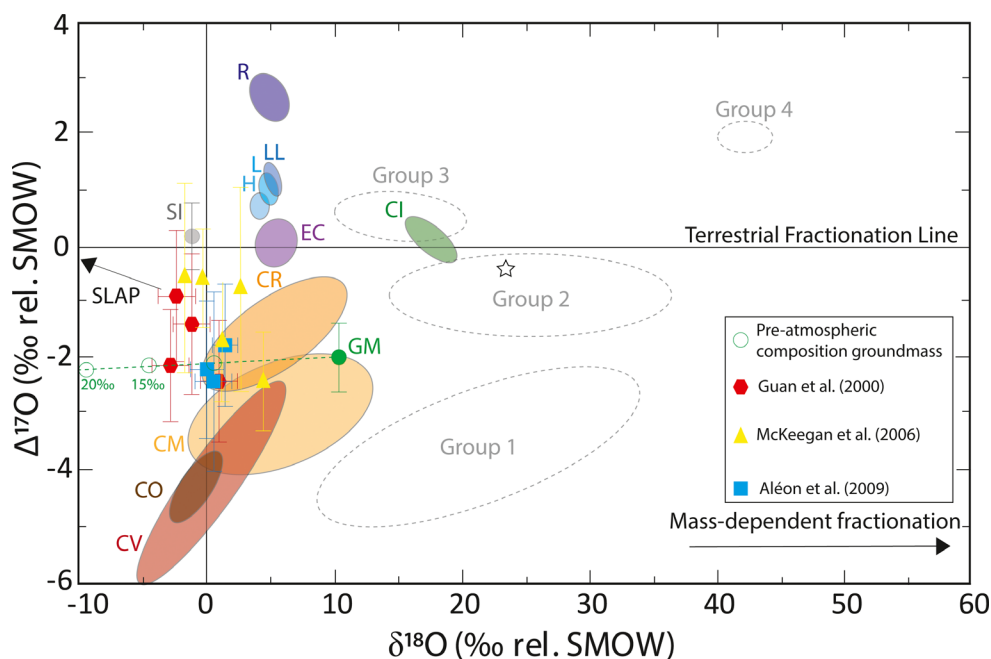
Fig. 12. Triple oxygen isotope diagram ($\Delta^{17}$O and $\delta^{18}$O) of the spherical inclusion (SI) and micrometeorite groundmass (GM). The spherical inclusion is located left of the enstatite chondrite (EC) field, while the micrometeorite groundmass is positioned near the CM chondrite field, offset to $\delta^{18}$O-enriched compositions. Micrometeoroids experience isotopic fractionation processes during atmospheric entry heating. Oxygen isotope ratios can be modified through (1) mass-dependent fractionation, moving the composition to the right of the diagram; (2) mixing with atmospheric oxygen (star symbol—Thiemens et al. 1995); and (3) interaction with Antarctic precipitation, as represented by standard light antarctic precipitation (SLAP). Bulk isotopic compositions of micrometeorites generally fall in four distinct groups (Group 1–4), associated with anhydrous carbonaceous chondrites, hydrated carbonaceous chondrites, ordinary chondrites, and a newly described population of $^{16}$O-poor material (group 4), the affinities of which are currently not well understood. The oxygen isotopic composition of multiple CAIs and a single Al-rich chondrule from the EET 87746, GRO 95517, and Sahara 97072 unequilibrated enstatite chondrites have been added for comparison (polygons—Guan et al. 2000). Oxygen isotopic data for anhydrous IDPs (squares—Aléon et al. 2009) and fragments from Comet 81P/Wild2 (triangles—McKeegan et al. 2006) have been added as well. The dashed line connecting the oxygen isotopic composition of the micrometeorite groundmass contains several hollow, green circles that represent a potential pre-atmospheric composition taking into account ~10, 15, and 20‰ of oxygen isotope fractionation processes. Figure modified from Suavet et al. (2010). Error bars represent the uncertainty on the $\Delta^{17}$O (2SE for micrometeorite WF1202A-001, anhydrous IDPs and Comet 81P/Wild2 fragments, 1SE for individual analyses from Guan et al. 2000) and $\delta^{18}$O ratio (1SE for individual analyses from Guan et al. 2000). (Color figure can be viewed at wileyonlinelibrary.com.)

In addition to olivine, WF1202A-001 also retained multiple, relict low-Ca pyroxene grains, as the average cooling rate of cosmic spherules kinetically inhibits the crystallization of neo-formed pyroxene phases (Taylor and Brownlee 1991). The relict nature of pyroxene in micrometeorite WF1202A-001 is also demonstrated by its highly refractory composition (Mg# = 99—see Fig. 9 and see Data S2). More specifically, the composition of this particular pyroxene is similar to those of highly refractory low-Fe, Cr-enriched (LICE) silicates (FeO/Cr$_2$O$_3$ < 1), previously reported on by Ebel et al. (2012) and Suttle et al. (2019a), which are typically associated with first-generation condensation-crystallized silicates and/or refractory CAIs. Both the relict olivine and pyroxene phases appear to be linked with CAIs.

We cannot verify whether the Ni-bearing sulfide phases in the micrometeorite groundmass are primary or were formed as a consequence of atmospheric entry heating. The latter process should be considered since high-Ni sulfide phases such as pentlandite can also be formed by cooling of high temperature Fe-Ni-S melts (Schrader et al. 2016). These types of melts may be produced due to the immiscibility of chalcophile and siderophile elements from the surrounding silicate melt when the precursor particle is melted during atmospheric entry (Genge and Grady 1998). Alternatively, if the Ni-bearing sulfide phases are primary, then this would suggest a contribution of oxidized chondrites such as the carbonaceous and R chondrites. The preservation of sulfide phases also implies that micrometeorite WF1202A-001 avoided significant weathering during its residence on Earth.
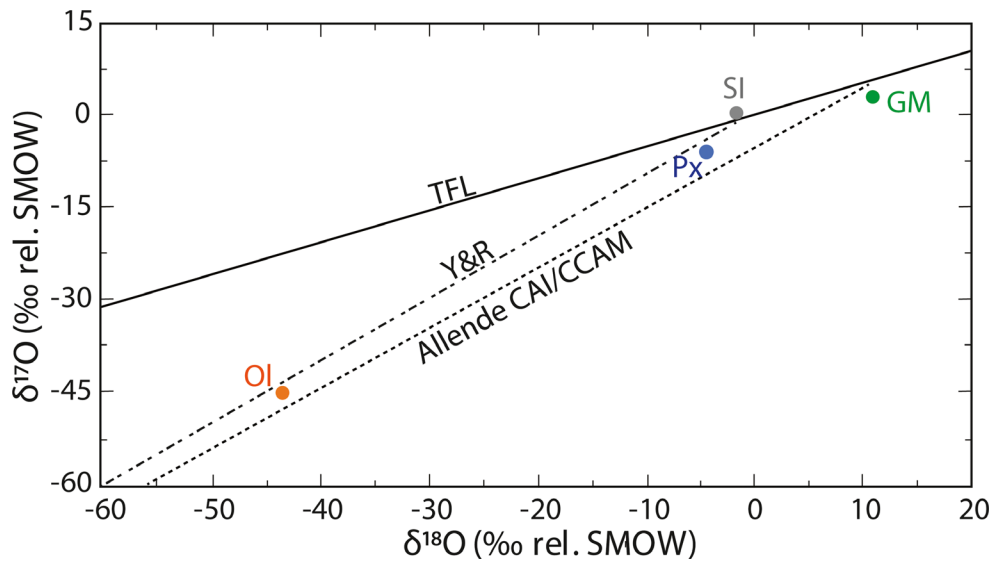
Fig. 13. Oxygen isotope diagram ($\delta^{17}O$ and $\delta^{18}O$) of coarse-grained olivine and low-Ca pyroxene in the micrometeorite groundmass. Both mineral phases are positioned in-between the Allende CAI line (Clayton et al. 1977) and the Y&R line (Young and Russell 1998). Olivine grains have $^{16}O$-rich compositions while the pyroxene has a more $^{16}O$-poor composition. The oxygen isotopic composition of the analyzed olivine is similar to that observed for refractory mineral phases (e.g., hibonite, melilite, etc.) in CAIs. (Color figure can be viewed at wileyonlinelibrary.com.)
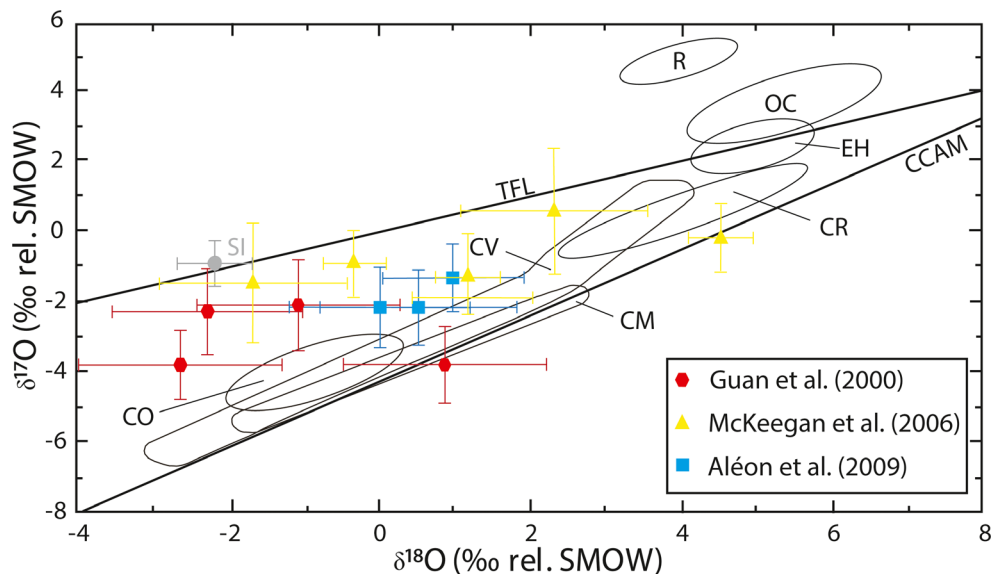


Fig. 14. Oxygen isotopic composition ($\delta^{17}O$ and $\delta^{18}O$) of the spherical inclusion (SI) in WF1202A-001. The range of oxygen isotopic compositions observed in chondrules from a large variety of chondritic meteorites are shown for comparison (Rubin 2000b). The chondrule does not plot close to any known chondrite field. The oxygen isotopic composition of multiple CAIs and a single Al-rich chondrule from the EET 87746, GRO 95517, and Sahara 97072 unequilibrated enstatite chondrites has been added for comparison (polygons—Guan et al. 2000). Oxygen isotopic data for anhydrous IDPs (squares—Aléon et al. 2009) and fragments from Comet 81P/Wild2 (triangles—McKeegan et al. 2006) have been added as well. Error bars represent the uncertainty on the $\delta^{17}O$ (2SE for micrometeorite WF1202A-001, anhydrous IDPs and Comet 81P/Wild2 fragments, 1SE for individual analyses from Guan et al. 2000) and $\delta^{18}O$ ratio (2SE for micrometeorite WF1202A-001, anhydrous IDPs and Comet 81P/Wild2 fragments, 1SE for individual analyses from Guan et al. 2000). Abbreviations: TFL = terrestrial fractionation line, CCAM = carbonaceous chondrite anhydrous mineral line (Clayton et al. 1977). (Color figure can be viewed at wileyonlinelibrary.com.)

## A Complete and Well-Preserved Chondrule within an Antarctic Micrometeorite

The physical, petrographic, and geochemical properties of the spherical inclusion bear a strong resemblance to chondrules observed in chondritic meteorites. Here, we discuss five parameters—size, shape, texture, mineralogy, and chemistry—supporting the identification of this inclusion as a chondrule.

Chondrule sizes range from tens of micrometers up to several millimeters depending on the class/group of chondrite, and may vary substantially among specific classes or groups of chondritic meteorites (see Jones 2012; Friedrich et al. [2015] for an overview). This variation has previously been attributed to an array of processes including chondrule formation, parent body alteration, or post-solidification nebular sorting (Shu et al. 1996; Weidenschilling 2000; Cuzzi et al. 2001; Cuzzi and Weidenschilling 2006; Chiang and Youdin 2010; Wurm et al. 2010). Combining the average chondrule size and texture can nevertheless provide important information toward the identification and classification of meteorites (Van Schmus and Wood 1967; Weisberg et al. 2006).

The maximum apparent size of the spherical inclusion is approximately 220 μm, which is consistent with average chondrule sizes in CM, CO, H, and EH chondrites (Table 1). Note, however, that chondrule sizes may vary considerably within specific types of chondritic meteorites and that average sizes may not be representative. While peak atmospheric temperatures likely exceeded 1400°C, which predominantly affects the glassy mesostasis (transitional window of glass ~650–850°C) within the spherical inclusion of micrometeorite WF1202A-001, we argue that the size of the chondrule did not change extensively. This is demonstrated by the sharp, well-defined contact between the spherical inclusion and the surrounding micrometeorite groundmass (Fig. 4). In addition, we observe neo-formed olivine phenocrysts and magnetite dendrites, which crystallized following quench-cooling during the later stages of atmospheric entry (Toppani et al. 2001) using the object's rim as substrate.

Second, the shape of the spherical inclusion is rounded and slightly elliptical ($\varepsilon = 1.12$), displaying a smooth surface across the entire object. Chondrules typically display (highly) irregular surfaces at the scale of ~50 μm (Grossman et al. 1988), but barred olivine and radial-pyroxene chondrules (including their respective fragments in micrometeorites) may often display smooth surfaces (Grossman et al. 1988; Genge et al. 2005). The presence of smooth surfaces among barred olivine and radial-pyroxene chondrules is consistent with their formation as igneous droplets with spherical shapes formed as a result of surface tension (Grossman et al. 1988; Genge et al. 2005).

Third, barred olivine textures among chondritic meteorites are predominantly observed within chondrules. Nonporphyritic chondrules, including barred olivine, cryptocrystalline, and radial pyroxene types, are typically outnumbered (~<10%) compared to porphyritic chondrules (Table 1). Nonporphyritic textures develop when the chondrule precursor is superheated above the liquidus, effectively destroying all crystal nuclei, and is subsequently cooled down at highly variable rates of ~500–3000 °C h$^{-1}$ for barred olivine textures (Desch and Connolly 2002). The nucleation of barred olivine and radial pyroxene chondrules presumably initiated after melt droplets collided with solid, neighboring grains (Connolly and Hewins 1995). The spherical depression with surrounding Cr-rich spinel grains in the spherical inclusion of micrometeorite WF1202A-001 may have hosted a solid (relict) grain that served as nucleation point for the barred olivine texture (Fig. 2).

Fourth, the mineral content of the spherical inclusion comprises common major and accessory mineral phases observed in chondrules, including olivine, Fe-Ni metal alloys, and Cr-rich spinel. Olivine crystals within the spherical inclusion are FeO-rich ($Fo_{63}$) and display normal zoning, while the interstitial mesostasis is more pyroxene-rich with clear enrichments in Si, Fe, Al, and Ca (Fig. 10).

Finally, the major elemental composition of the spherical inclusion appears to be very similar to, for example, porphyritic chondrules from the LL 3.00 Semarkona meteorite (Jones 1990), with the exception of a minor enrichment in Mn (within uncertainty) and a large depletion in Na and K (Fig. 11). The depletion of moderately volatile elements in the spherical inclusion is likely a result of atmospheric entry heating, similar to the micrometeorite groundmass, as observed from the presence of vesicles near the inclusion's margin (Fig. 2). The REE pattern of the spherical inclusion is consistent with a mixture of olivine (subchondritic) and glassy mesostasis (suprachondritic) in chondrules, where olivine is more significant (~70–80 area%) than the glassy mesostasis (Figs. 2 and 6). This may explain the overall subchondritic REE signature of the spherical inclusion.

Based on the physical, petrographic, mineralogical, and chemical properties of the spherical inclusion described above, we interpret this phase as a well-preserved chondrule.

## Oxygen Isotopic Composition of Micrometeorite WF1202A-001: A Link to IDPs and Cometary Bodies?

Apart from the textural and geochemical modifications that extraterrestrial dust particles experience during atmospheric entry heating, oxygen

isotope ratios also undergo significant changes. Previous isotopic studies on cosmic spherules (Yada et al. 2005; Suavet et al. 2010; Van Ginneken et al. 2017; Goderis et al. 2020; Rudraswami et al. 2020; Suttle et al. 2020) have demonstrated that the atmospheric entry of micrometeorites results in two main isotopic overprints. First, a mass-dependent fractionation effect arises due to flash heating and results in a proportional $\delta^{18}O$ enrichment. Second, once molten, the particle experiences a progressive isotopic exchange with stratospheric (terrestrial) oxygen. This causes the particle's bulk composition to approach stratospheric oxygen values with a $\delta^{17}O$ of 11.8‰ and $\delta^{18}O$ of 23.5‰ (Thiemens et al. 1995). Suavet et al. (2010) argued that the extent of both processes positively correlates with the texture (and thus maximum heating temperature) of cosmic spherules. Consequently, the effects of oxygen isotopic fractionation and mixing on the final oxygen isotopic composition of micrometeorites should increase from porphyritic over barred olivine and cryptocrystalline to vitreous textures. Rudraswami et al. (2020) furthermore argue that mass-dependent fractionation processes dominate over atmospheric oxygen mixing.

Micrometeorite WF1202A-001 displays a microporphyritic texture, implying a fairly limited shift in the bulk oxygen isotopic composition of this particle. This appears to be the case since the oxygen isotopic composition of the groundmass of micrometeorite WF1202A-001 is positioned at the edge of the CM chondrite field (Fig. 12). Since we cannot quantify the extent of mass-dependent fractionation processes and mixing with atmospheric oxygen, the primordial bulk or matrix oxygen isotopic compositions of micrometeorite WF1202A-001 are difficult to determine. Clayton et al. (1986) observed average shifts in $\delta^{18}O$ values of ~8‰ for iron fusion crusts arising due to mixing with atmospheric oxygen and kinetic effects. Suavet et al. (2010) observed overall larger amounts of fractionation and mixing ranging from ~10 to 50‰ in cosmic spherules from the Transantarctic Mountains. Recently, Rudraswami et al. (2020) have determined the average increase in $\delta^{18}O$ values for a series of cosmic spherules spanning a large textural range. They observed average increases of +12‰, +20‰, +22‰, +25‰, +26‰, and +50‰ for cosmic spherules in the following order: scoriaceous < porphyritic < barred olivine < cryptocrystalline < vitreous < CAT. Hence, the original $\delta^{18}O$ value of micrometeorite WF1202A-001 may have shifted up to ~10–20‰. By applying an ~15‰ offset to the oxygen isotopic composition of the micrometeorite groundmass, its original oxygen isotopic composition was presumably positioned left of the carbonaceous chondrite fields. Such composition is similar to values

reported by Guan et al. (2000), McKeegan et al. (2006), and Aléon et al. (2009) for CAIs and an Al-rich chondrule from the EET 87746, GRO 95517, and Sahara 97072 unequilibrated enstatite chondrites; fragments from Comet 81P/Wild2; and chondritic anhydrous interplanetary dust particles, respectively (see below and Fig. 12). However, since the original oxygen isotopic composition of the micrometeorite precursor body is unknown, and the contribution of mass-dependent fractionation and mixing processes cannot be quantified accurately, this estimate should be considered with care.

The relict olivine grain (Ol1) displays extreme $^{16}O$-rich compositions, with a $\delta^{17}O$ of –45.8‰ and $\delta^{18}O$ of –43.7‰, preserving primordial solar-like values identical to those found in CAIs (Clayton and Mayeda 1999; Yurimoto et al. 2008; Fig. 13). These values imply that Ol1 formed as a primitive first-generation condensation-crystallized silicate, which survived accretion, parent body alteration, liberation into interplanetary space, atmospheric entry, and terrestrial residence without any significant isotopic overprinting.

In contrast, the large low-Ca pyroxene grain (Px1) plots closer to the intersection with the terrestrial fractionation line (TFL; Fig. 13). Such compositions are also commonly found in chondritic meteorites and can best be explained by isotopic mixing between first-generation silicates and later $^{18}O$-rich materials. Mixing may have occurred in a transient melting scenario with either accreted volatile dust or by exchange with surrounding $SiO_2$ gas (McKeegan et al. 1998; Krot et al. 2005). Thus, Px1 was most likely inherited from either a fragmented type II chondrule or igneous CAI. Micrometeorite WF1202A-001 therefore appears to contain an appreciable amount (~5–10 area%) of CAI-derived material. However, due to the fairly small size of micrometeorites in comparison with their respective parent bodies, we cannot verify whether the importance of CAI-derived material is representative.

The unique and anomalous oxygen isotopic composition ($\delta^{17}O$ of –0.98‰, $\delta^{18}O$ of –2.16‰, and $\Delta^{17}O$ of 0.15‰) of the chondrule in micrometeorite WF1202A-001 is puzzling since none of the known chondrite groups (including their individual components) matches its composition (Greenwood et al. 2020). Based on petrographic observations, we argue that atmospheric melting of the chondrule within micrometeorite WF1202A-001 was limited to its glassy mesostasis. This occurs at temperatures exceeding the glass transitional window (650–850°C) and results in oxidative volatilization of reduced, volatile compounds, and diffusive exchange with the surrounding (molten) silicate groundmass. The former process is demonstrated by the presence of rounded vesicles near

the chondrule's margin (Fig. 2) and the overall depletion of volatile elements such as Na and K (Fig. 11). The latter process is illustrated by the development of microscopic magnetite grains due to the oxidation of Fe-Ni metal (Fig. 2). Both processes have previously been inferred from meteorite fusion crusts (Genge and Grady 1999) and igneous rims in scoriaceous and unmelted micrometeorites (Genge et al. 2005; Genge 2006). We can therefore argue that at least a limited amount of chemical and isotopic modification has taken place, yet the extent of these processes remains difficult to quantify. Since mass-dependent fractionation and/or mixing processes tend to shift the original oxygen isotopic composition of dust particles toward higher $\delta^{18}O$ values, this would imply that the original oxygen isotopic composition of the chondrule was even more $^{18}O$–depleted. This underlines the anomalous isotopic signature of the chondrule.

Due to its position close to the terrestrial fractionation line, we should also consider a possible contribution of standard light Antarctic precipitation (SLAP—Fig. 12). This isotopic reservoir can modify the oxygen isotopic composition of micrometeorites as a result of aqueous alteration at the Earth's surface (see e.g., Van Ginneken et al. 2016). According to Zekollari et al. (2019), the oxygen isotopic composition of the surrounding Nansen blue ice field is $\sim-43 \pm 3$ ‰ (1SD). To produce the anomalous oxygen isotopic composition observed in the chondrule starting from a hypothetical CM-like composition (mean $\delta^{18}O$ of $+9$‰, and $\Delta^{17}O$ of $-2.3$‰, n = 34; Clayton and Mayeda 1999), we would require a SLAP contribution of ~22%, leading to a distinct $\Delta^{17}O$ of $-1.9$‰, which is inconsistent with the isotopic composition of the chondrule. Such large contribution is also unlikely since weathering features (e.g., dissolution, secondary mineral phases) in micrometeorite WF1202A-001 are absent (Van Ginneken et al. 2016). In addition, the presence of sulfide phases and the preservation of the glassy mesostasis within the micrometeorite groundmass, both of which are highly susceptible to terrestrial weathering, support this assumption (e.g., Fig. 2).

A potential solution is provided by Guan et al. (2000) who investigated the oxygen isotopic composition of multiple CAIs and a single Al-rich chondrule from the EET 87746, GRO 95517, and Sahara 97072 unequilibrated enstatite chondrites. They have reported similar values (within uncertainty) for both the CAI (mixtures of melilite, spinel, perovskite, hibonite, etc.) and chondrule (spinel and glass from Al-rich chondrule) components as micrometeorite WF1202A-001. Hence, this might suggest that the chondrule in micrometeorite WF1202A-001 may have been inherited from enstatite chondrites. However, this is rather unlikely since the chondrule was relatively enriched in FeO, and lithophile elements were essentially absent from the Fe-Ni nodules, inconsistent with the highly reduced nature of enstatite chondrites.

Alternatively, the chondrule may affiliate to anhydrous IDPs and fragments from Comet 81P/Wild 2, which display comparable oxygen isotopic ratios (Figs. 12 and 13). Interestingly, the estimated pre-atmospheric oxygen isotopic composition of the micrometeorite groundmass is also positioned in proximity of these "cometary fields" when the extent of mass-dependent fractionation processes ranges from ~5 to 15‰. Micrometeorite WF1202A-001 may possibly have sampled a carbonaceous chondrite parent body, analogous to, but distinct from CM, CO, or CV chondrites based on the major element composition of the groundmass, chondrule size, and the oxygen isotopic systematics. In addition, these results may suggest a genetic link between carbonaceous chondrites and cometary bodies (such as Comet 81P/Wild2) given their comparable oxygen isotope compositions.

The implications of these results are twofold. First, the diversity among solar system materials is much larger than our contemporary (micro)meteorite inventory suggests (see also, e.g., Yada et al. 2005; Gounelle et al. 2009; Suavet et al. 2010; Cordier and Folco 2014; Van Ginneken et al. 2017; Goderis et al. 2020; Suttle et al. 2020). Second, the classical dichotomy (i.e., carbonaceous versus noncarbonaceous chondrites) observed in oxygen isotope space should be reconsidered as the oxygen isotope compositions of carbonaceous chondrites appear to be much more diverse (see also e.g., Goodrich et al. 2019; Kebukawa et al. 2019; King et al. 2019; Kerraouch et al. 2020; Suttle et al. 2020). Micrometeorite WF1202A-001 may thus possibly serve as an example for the (hidden) diversity present among the carbonaceous chondrite class.

## The Atmospheric Entry History and Source Region of Micrometeorite WF1202A-001

The preservation of a complete chondrule within micrometeorite WF1202A-001 is unique as asteroids are subjected to a range of collisional events and alteration processes throughout their residence in the solar system. Based on previous studies regarding the behavior of shock waves in heterogeneous media (e.g., Melosh 1996; Ernstson et al. 2001), Genge et al. (2005) proposed that dust production predominantly affects chondrules due to their higher shock impedance with respect to the chondritic matrix. Since particle and shock wave velocities migrate faster through denser materials, chondrules tend to fragment more easily. In addition,

chondrule fragmentation may also be amplified by the buildup of heterogeneous peak pressures originating from the reflection and refraction of shock waves at the border between high (cfr. chondrule) and low (cfr. matrix) shock density materials.

Aqueous alteration on parent asteroids may also play a pivotal role in the removal or alteration of chondrules (e.g., Bunch and Chang 1980; Richardson 1981; Ikeda 1983; Tomeoka and Buseck 1985; Hanowski and Brearley 1997, 2001). This is further supported by Suttle et al. (2019b) who argued that chondrules are predominantly replaced by phyllosilicates in hydrated carbonaceous chondrites (e.g., CI, CM, CR) based on a study of scoriaceous and unmelted micrometeorites.

In addition, chondrule(s) (fragments) are also subjected to temperatures up to 1700°C as a result of atmospheric entry heating (Love and Brownlee 1991). The preservation of relict mineral phases in micrometeorite WF1202A-001 such as olivine (melting point at atmospheric pressure: 1890°C) and low-Ca pyroxene (1557°C) suggests that peak atmospheric temperatures were likely not as high, but sufficient to exceed the solidus of chondritic matrix (~1400°C; Toppani et al. 2001). According to Hewins and Radomsky (1990), chondrule liquidus temperatures range between ~1200 and 1900°C, and display a peak in the distribution at ~1500–1550°C for barred olivine textures (Radomsky and Hewins 1990; Yu and Hewins 1998). The peak atmospheric temperature experienced by micrometeorite WF1202A-001 therefore appears to range between 1400 and 1550°C. Note, however, that the chondrule's glassy mesostasis must have melted as the transitional window of glass is situated between 650 and 850°C.

Atmospheric entry heating also governs the size of micrometeorites (Love and Brownlee 1991; Genge and Grady 1998; Genge 2017). During atmospheric entry, a number of competing processes (e.g., evaporation, vesiculation, ejection of high-density sidero- and chalcophile elements, etc.) induce volumetric changes in the micrometeorite precursor particle. On average, micrometeorite precursors are estimated to have been ~1.5–2 times larger than the resulting, recrystallized micrometeorite recovered on Earth as a consequence of evaporative processes (Love and Brownlee 1991). The volumetric effects of vesiculation are more difficult to determine but are mostly relevant for phyllosilicate-bearing precursor particles (Genge 2017). Here, we will only consider the effects of evaporation to calculate the original size of micrometeorite WF1202A-001. This information is relevant to re-create the atmospheric entry history (i.e., entry speed, angle, etc.) of micrometeorite WF1202A-001 and serves to identify its source region within the solar system. We estimate that the original

micrometeoroid size ranged from 650 to 850 μm, and that the chondrule size did not change extensively over the course of its atmospheric entry (see earlier).

The fairly large (original) size of micrometeorite WF1202A-001 suggests that the initial atmospheric entry velocity is likely to be asteroidal (~12–15 km s$^{-1}$) rather than cometary (~20 km s$^{-1}$), since larger dust particles are more prone to melting (Love and Brownlee 1991). In addition, the entry angle of micrometeorite WF1202A-001 was presumably close to the horizontal (90°) as this has a moderating effect on the peak atmospheric temperature experienced, relative to the vertical (0°). Micrometeorite WF1202A-001 therefore likely originated from the main belt asteroids, since particles >20 μm with average (long-period) cometary velocities (i.e., 20 km s$^{-1}$) are not expected to survive atmospheric entry (Love and Brownlee 1991). However, the particle may also have originated from the JFCs, such as Comet 81P/Wild2, which are short period comets that orbit the Sun in a timespan of less than 20 years. The JFC population have low eccentricities and inclination angles that produce low-velocity dust particles, analogous to main belt asteroids that promote atmospheric survival. Based on numerical modeling, Nesvorný et al. (2010) concluded that dust from the inner solar system is predominantly sourced from the JFC. We therefore suggest that micrometeorite WF1202A-001 likely originated either from a main belt asteroid or JFC, and entered Earth's atmosphere at asteroidal velocities (12–15 km s$^{-1}$) and a near horizontal angle.

## CONCLUSION

Particle WF1202A-001 is a microporphyritic cosmic spherule from the Sør Rondane Mountain micrometeorite collection that contains relict MgO-rich olivine and low-Ca pyroxene grains, as well as a spherical inclusion, interpreted as a barred olivine chondrule. While the micrometeorite's groundmass melted almost entirely, its bulk geochemical composition is relatively well preserved and consistent with a chondritic parent body, possibly from CM or CV lineage. This is supported by oxygen isotope ratio data, which are consistent with a carbonaceous chondritic precursor body. Micrometeorite WF1202A-001 appears to contain an appreciable amount (~5–10 area%) of CAI-derived material, including forsterite (Fo$_{98-99}$) and enstatite (En$_{99}$Wo$_1$) grains. At least one olivine grain exhibits extremely negative solar-like values ($\delta^{17}$O ≈ $\delta^{18}$O ≈ –45‰), reminiscent of primitive first-generation condensation-crystallized silicates. Low-Ca pyroxene plots much closer to the terrestrial fractionation line— interpreted to represent mixing between first-generation

silicates and later accreted ^{18}O-rich volatile dust or exchange with $SiO_2$ gas. As a result, the low-Ca pyroxene grain was presumably inherited from type II chondrules or igneous CAIs.

The chondrule displays a barred olivine texture that is embedded in a glassy mesostasis. Its bulk composition is consistent with type II chondrules observed in chondritic meteorites. However, its oxygen isotopic composition is anomalous, plotting near the terrestrial fractionation line, offset to a lower $\delta^{18}O$ relative to the enstatite chondrite field, and incompatible with known chondritic materials. While the chondrule's glassy mesostasis has melted and recrystallized during atmospheric entry, allowing for chemical and isotopic interaction, the combined effects of mass-dependent fractionation and mixing with atmospheric oxygen cannot account for the chondrule's anomalous oxygen isotopic composition. Due to the lack of weathering features in micrometeorite WF1202A-001, we believe the contribution of SLAP is negligible. The chondrule's oxygen isotopic composition is, however, comparable to those observed for anhydrous IDPs and fragments from Comet 81P/Wild2. Consequently, we propose that micrometeorite WF1202A-001 sampled a new type of carbonaceous chondrite parent body that can potentially be linked to cometary bodies.

The peak atmospheric temperature experienced by micrometeorite WF1202A-001 presumably ranged between 1400 and 1550°C based on the melting point of the respective micrometeorite components. Additionally, the fairly large size of micrometeorite WF1202A-001 suggests low, asteroidal entry velocities (12–15 km s$^{-1}$) with an inclination angle close to the horizontal (~80°). Such parameters are consistent with cosmic dust originating from low eccentricity, low inclination source regions, which include both the main belt asteroids and the JFCs.

*Editorial Handling*—Dr. Donald Brownlee

## REFERENCES

Aléon J., Engrand C., Leshin L. A., and McKeegan K. D. 2009. Oxygen isotopic composition of chondritic interplanetary dust particles: A genetic link between carbonaceous chondrites and comets. *Geochimica et Cosmochimica Acta* 73:4558–4575.

Bunch T. E. and Chang S. 1980. Carbonaceous chondrites-II. Carbonaceous chondrite phyllosilicates and light element geochemistry as indicators of parent body processes and surface conditions. *Geochimica et Cosmochimica Acta* 44:1543–1577.

Chiang E. and Youdin A. 2010. Forming planetesimals in solar and extrasolar nebulae. *Annual Review of Earth and Planetary Sciences* 38:493–522.

Ciesla F. J. and Hood L. L. 2002. The nebular shock wave model for chondrule formation: Shock processing in a particle-gas suspension. *Icarus* 158:281–293.

Clayton R. N. 1993. Oxygen isotopes in meteorites. *Annual Reviews in Earth and Planetary Sciences* 21:115–149.

Clayton R. N. and Mayeda T. K. 1999. Oxygen isotope studies of carbonaceous chondrites. *Geochimica et Cosmochimica Acta* 63:2089–2104. https://doi.org/10.1016/S0016-7037(99)00090-3

Clayton R. N., Onuma N., Grossman L., and Mayeda T. K. 1977. Distribution of the pre-solar component in Allende and other carbonaceous chondrites. *Earth and Planetary Science Letters* 34:209–224.

Clayton R. N., Mayeda T. K., and Brownlee D. E. 1986. Oxygen isotopes in deep-sea spherules. *Earth and Planetary Science Letters* 79:235–240.

Connolly C. H. Jr. and Hewins R. H. 1995. Chondrules as products of dust collisions with totally molten droplets within a dust-rich nebular environment: An experimental investigation. *Geochimica et Cosmochimica Acta* 59:3131–3246.

Connolly C. H. Jr. and Love S. G. 1998. The formation of chondrules: Petrologic tests of the shock wave model. *Science* 280:62–67.

Cordier C. and Folco L. 2014. Oxygen isotopes in cosmic spherules and the composition of the near Earth interplanetary dust complex. *Geochimica et Cosmochimica Acta* 146:18–26.

Cordier C., Folco L., Suavet C., Sonzogni C., and Rochette P. 2011. Major, trace element and oxygen isotope study of glass cosmic spherules of chondritic composition: The record of their source material and atmospheric entry heating. *Geochimica et Cosmochimica Acta* 75:5203–5218.

Cordier C., Suavet C., Folco L., Rochette P., and Sonzogni C. 2012. HED-like cosmic spherules from the Transantarctic Mountains, Antarctica: Major and trace element abundances and oxygen isotopic compositions. *Geochimica et Cosmochimica Acta* 77:515–529.

Cuzzi J. N. and Weidenschilling S. J. 2006. Particle-gas dynamics and primary accretion. In *Meteorites and the*

*early solar system II*, edited by Lauretta D. S. and McSween H. Y. Tucson, Arizona: The University of Arizona Press. pp. 353–382.

Cuzzi J. N., Hogan R. C., Paque J. M., and Dobrovolskis A. R. 2001. Size selective concentration of chondrules and other small particles in protoplanetary nebula turbulence. *Astrophysical Journal* 546:496–508.

Das G. R., Banerjee A., Goderis S., Claeys P., Vanhaecke F., and Chakrabarti R. 2017. Evidence for a chondritic impactor, evaporation-condensation effects and melting of the Precambrian basement beneath the "target" Deccan basalts at Lonar crater, India. *Geochimica et Cosmochimica Acta* 215:51–75.

Desch S. J. and Connolly C. H. Jr. 2002. A model of the thermal processing of particles in solar nebula shocks: Application to the cooling rates of chondrules. *Meteoritics & Planetary Science* 37:183–207.

Dionnet Z., Suttle M. D., Longobardo A., Rotundi A., Folco L., Della C. V., and King A. 2020. X-ray computed tomography: Morphological and porosity characterization of giant Antarctic micrometeorites. *Meteoritics & Planetary Science* 55:1581–1599.

Ebel D. S., Weisberg M. K., and Beckett J. R. 2012. Thermochemical stability of low-iron, manganese-enriched olivine in astrophysical environments. *Meteoritics & Planetary Science* 47:585–593.

Engrand C. and Maurette M. 1998. Carbonaceous micrometeorites from Antarctica. *Meteoritics & Planetary Science* 33:565–580.

Engrand C., McKeegan K. D., Leshin L. A., Herzog G. F., Schnabel C., Nyquist L. E., and Brownlee D. E. 2005. Isotopic compositions of oxygen, iron, chromium and nickel in cosmic spherules: Toward a better comprehension of atmospheric entry heating effects. *Geochimica et Cosmochimica Acta* 69:5365–5385.

Ernstson K., Rampino N. R., and Hiltl M. 2001. Cratering of cobbles in Triassic Bundsandstein conglomerates in NE Spain: Shock deformation of in situ deposits in the vicinity of large impacts. *Geology* 29:11–14.

Flynn G. J., Durda D. D., Sandel L. E., Kreft J. W., and Strait M. M. 2009. Dust production from the hypervelocity impact disruption of the Murchison hydrous CM2 meteorite: Implications for the disruption of hydrous asteroids and the production of interplanetary dust. *Planetary and Space Science* 57:119–126.

Folco L. and Cordier C. 2015. Micrometeorites. *European Mineralogical Union Notes in Planetary Mineralogy* 15:253–297. https://doi.org/10.1180/EMU-notes15.9.

Folco L., Rochette P., Perchiazzi N., D'Orazio M., Laurenzi M., and Tiepolo M. 2008. Microtektites from Victoria land transantarctic mountains. *Geology* 36:291–294.

Friedrich J. M., Weisberg M. K., Ebel D. S., Biltz A. E., Corbett B. M., Iotzov I. V., Khan W. S., and Wolman M. D. 2015. Chondrule size and related physical properties: A compilation and evaluation of current data across all meteorite groups. *Chemie der Erde* 75:419–443.

Genge M. J. 2006. Igneous rims on micrometeorites. *Geochimica et Cosmochimica Acta* 70:2603–2621.

Genge M. J. 2017. An increased abundance of micrometeorites on Earth owing to vesicular parachutes. *Geophysical Research Letters* 44:1679–1686.

Genge M. J. and Grady M. M. 1998. Melted micrometeorites from Antarctic ice with evidence for the separation of immiscible Fe-Ni-S liquids during entry heating. *Meteoritics & Planetary Science* 33:425–434.

Genge M. J. and Grady M. M. 1999. The fusion crusts of stony meteorites: Implications for the atmospheric reprocessing of extraterrestrial materials. *Meteoritics & Planetary Science* 34:341–356.

Genge M. J., Grady M. M., and Hutchinson R. 1997. The textures and compositions of fine-grained Antarctic micrometeorites: Implications for comparisons with meteorites. *Geochimica et Cosmochimica Acta* 61:5149–5162.

Genge M. J., Gileski A., and Grady M. M. 2005. Chondrules in Antarctic micrometeorites. *Meteoritics & Planetary Science* 40:225–238.

Genge M. J., Engrand C., Gounelle M., and Taylor S. 2008. The classification of micrometeorites. *Meteoritics & Planetary Science* 43:497–515.

Genge M. J., Suttle M., and Van Ginneken M. 2016. Olivine settling in cosmic spherules during atmospheric deceleration: An indicator of the orbital eccentricity of interplanetary dust. *Geophysical Research Letters* 43:10,646–10,653.

Genge M. J., Suttle M., and Van Ginneken M. 2017. Thermal shock fragmentation of Mg silicates within scoriaceous micrometeorites reveal hydrated asteroidal sources. *Geology* 45:891–894.

Goderis S., Soens B., Huber M. S., McKibbin S., Van Ginneken M., Debaille V., Greenwood R. C., Franchi I. A., Cnudde V., Van Malderen S., Vanhaecke F., Koeberl C., Topa D., and Claeys P. H. 2020. *Geochimica et Cosmochimica Acta* 270:112–143.

Gooding J. L., Keil K., and Healy J. T. 1978. Physical properties of individual chondrules from ordinary chondrites (abstract). *Meteoritics* 13:476–477.

Gooding J. L., Keil K., Fukuoka T., and Schmitt R. A. 1980. Elemental abundances in chondrules from unequilibrated chondrites: Evidence for chondrule origin by melting of pre-existing materials. *Earth and Planetary Science Letters* 50:171–180.

Goodrich C. A. and Delaney J. S. 2000. Fe/Mg-Fe/Mn relations of meteorites and primary heterogeneity of primitive achondrite parent bodies. *Geochimica et Cosmochimica Acta* 64:149–160.

Goodrich C. A., Zolensky M. E., Fioretti A. M., Shaddad M. H., Downes H., Hiroi T., Kohl I., Young E. D., Kita N. T., Hamilton V. E., Riebe M. E. I., Busemann H., Macke R. J., Fries M., Ross D. K., and Jenniskens P. 2019. The first samples from Almahata Sitta showing contacts between ureilitic and chondritic lithologies: Implications for the structure and composition of asteroid 2008 TC$_3$. *Meteoritics & Planetary Science* 54:2769–2813.

Gounelle M., Chaussidon M., Morbidelli A., Barrat J.-A., Engrand C., Zolensky M. E., and McKeegan K. D. 2009. A unique basaltic micrometeorite expands the inventory of solar system planetary crusts. *Proceedings of the National Academy of Sciences of the United States of America* 106:6904–6909.

Greenwood R. C., Burbine T. H., and Franchi I. A. 2020. Linking asteroids and meteorites to the primordial planetesimal population. *Geochimica et Cosmochimica Acta* 277:377–406.

Grossman J. N., Rubin A. E., Nagahara H., and King E. A. 1988. Properties of chondrules. In *Meteorites and the early solar system*, edited by Kerridge J. F. and Matthews M. S.

Tucson, Arizona: The University of Arizona Press. pp. 619–659.

Guan Y., McKeegan K. D., and MacPherson G. J. 2000. Oxygen isotopes in calcium-aluminum-rich inclusions from enstatite chondrites: new evidence for a single CAI source in the solar nebula. *Earth and Planetary Science Letters* 181:271–277.

Haba M. K., Yamaguchi A., Kagi H., Nagao K., and Hidaka H. 2017. Trace element composition and U-Pb age of zircons from Estherville: Constraints on the timing of the metal-silicate mixing event on the mesosiderite parent body. *Geochimica et Cosmochimica Acta* 215:76–91.

Hanowski N. P. and Brearley A. J. 1997. Chondrule serpentines as indicators of aqueous alteration in CM carbonaceous chondrites (abstract). 28th Lunar and Planetary Science Conference. CD-ROM.

Hanowski N. P. and Brearley A. J. 2001. Aqueous alteration of chondrules in CM carbonaceous chondrite, Allan Hills 81002: Implications for parent body alteration. *Geochimica et Cosmochimica* 65:495–518.

Herbst W. and Greenwood J. P. 2016. A new mechanism for chondrule formation: Radiative heating by hot planetesimals. *Icarus* 267:364–367.

Hewins R. H. 1996. Chondrules and the protoplanetary disk: An overview. In *Chondrules and the protoplanetary disk*, edited by Hewins R. H., Jones R. H., and Scott E. R. D. Cambridge: Cambridge University Press. pp. 3–9.

Hewins R. H. and Connolly C. H. Jr. 1996. Peak temperatures of flash-melted chondrules. In *Chondrules and the protoplanetary disk*, edited by Hewins R. H., Jones R. H., and Scott E. R. D. Cambridge: Cambridge University Press. pp. 197–204.

Hewins R. H. and Radomsky P. M. 1990. Temperature conditions for chondrule formation. *Meteoritics* 25:309–318.

Ikeda Y. 1983. Alteration of chondrules and matrices in the four Antarctic carbonaceous chondrites ALH-77307(C3), Y-790123(C2), and Y-74662(C3). *Memoirs of the National Institute of Polar Research Special Issue* 30:93–108.

Jacquet E., Alard O., and Gounelle M. 2015. Trace element geochemistry of ordinary chondrite chondrules: The type I/type II chondrule dichotomy. *Geochimica et Cosmochimica Acta* 155:47–67.

Johnson B. C., Minton D. A., Melosh H. J., and Zuber M. T. 2015. Impact jetting as the origin of chondrules. *Nature* 517:339–341.

Jones R. H. 1990. Petrology and mineralogy of Type II, FeO-rich chondrules in Semarkona (LL3.0): Origin by closed-system fractional crystallization, with evidence for supercooling. *Geochimica et Cosmochimica Acta* 54:1785–1802.

Jones R. H. 2012. Petrographic constraints on the diversity of chondrule reservoirs in the protoplanetary disk. *Meteoritics & Planetary Science* 47:1176–1190.

Kallemeyn G. W. and Wasson J. T. 1981. The compositional classification of chondrites: I. The carbonaceous chondrite groups. *Geochimica et Cosmochimica Acta* 45:1217–1230.

Kallemeyn G. W. and Wasson J. T. 1982. The compositional classification of chondrites: III. Ungrouped carbonaceous chondrites. *Geochimica et Cosmochimica Acta* 46:2217–2228.

Kallemeyn G. W. and Wasson J. T. 1985. The compositional classification of chondrites: IV. Ungrouped chondritic

meteorites and clasts. *Geochimica et Cosmochimica Acta* 49:261–270.

Kallemeyn G. W., Boynton W. V., Willis J., and Wasson J. T. 1978. Formation of the Bencubbin polymict meteoritic breccia. *Geochimica et Cosmochimica Acta* 42:507–515.

Kallemeyn G. W., Rubin A. E., Wang D., and Wasson J. T. 1989. Ordinary chondrites: Bulk compositions, classification, lithophile-element fractionations, and composition-petrographic type relationships. *Geochimica et Cosmochimica Acta* 53:2747–2767.

Kallemeyn G. W., Rubin A. E., and Wasson J. T. 1991. The compositional classification of chondrites: V. The Karoonda (CK) group of carbonaceous chondrites. *Geochimica et Cosmochimica Acta* 55:881–892.

Kallemeyn G. W., Rubin A. E., and Wasson J. T. 1994. The compositional classification of chondrites: VI. The CR carbonaceous chondrite group. *Geochimica et Cosmochimica Acta* 58:2873–2888.

Kallemeyn G. W., Rubin A. E., and Wasson J. T. 1996. The compositional classification of chondrites: VII. The R chondrite group. *Geochimica et Cosmochimica Acta* 60:2243–2256.

Kamei A., Horie K., Owada M., Yuhara M., Nakano N., Osanai Y., Adachi T., Hara Y., Terao S., Teuchi T., Shimura T., Tsukada K., Hokada T., Iwata C., Shiraishi K., Ishizuka H., and Takahashi Y. 2013. Late Proterozoic juvenile arc metatonalite and adakitic intrusions in the Sør Rondane Mountains, eastern Dronning Maud Land, Antarctica. *Precambrian Research* 234:47–62.

Kebukawa Y., Ito M., Zolensky M. E., Greenwood R. C., Rahman Z., Suga H., Nakato A., Chan Q. H. S., Fries M., Takeichi Y., Takahashi Y., Mase K., and Kobayashi K. 2019. A novel organic-rich meteoritic clast from the outer solar system. *Scientific Reports* 9:3169.

Kerraouch I., Bischoff A., Zolensky M. E., Pack A., Patzek M., Wölfer E., Burkhardt C., and Fries M. 2020. Characteristics of a new carbonaceous, metal-rich lithology found in the carbonaceous chondrite breccia Aguas Zarcas (abstract #2011). 51st Lunar and Planetary Science Conference. CD-ROM.

King A. J., Bates H. C., Krietsch D., Busemann H., Clay P. L., Schofield P. F., and Russell S. S. 2019. The Yamato-type (CY) carbonaceous chondrite group: Analogues for the surface of asteroid Ryugu? *Geochemistry* 79:125531.

Kojima S. and Shiraishi K. 1986. Note on the geology of the western part of the Sør Rondane Mountains, East Antarctica. *Memoirs of National Institute of Polar Research* 43:116–131.

Krot A. N., Fagan T. J., Nagashima K., Petaev M. I., and Yurimoto H. 2005. Origin of low-Ca pyroxene in amoeboid olivine aggregates: Evidence from oxygen isotopic compositions. *Geochimica et Cosmochimica Acta* 69:1873–1881.

Kurat G., Koeberl C., Presper T., Brandstätter F., and Maurette M. 1994. Petrology and geochemistry of Antarctic micrometeorites. *Geochimica et Cosmochimica Acta* 58:3879–3904.

Lodders K. 2003. Solar system abundances and condensation temperatures of the elements. *The Astrophysical Journal* 591:1220–1247.

Lofgren G. 1996. A dynamic crystallization model for chondrule melts. In *Chondrules and the protoplanetary disk*,

edited by Hewins R. H., Jones R. H., and Scott E. R. H. Cambridge: Cambridge University Press. pp. 187–196.

Lofgren G. and Russell W. J. 1986. Dynamic crystallization of chondrule melts of porphyritic and radial pyroxene composition. *Geochimica et Cosmochimica Acta* 50:1715–1726.

Love S. G. and Brownlee D. E. 1991. Heating and thermal transformation of micrometeoroids entering the Earth's atmosphere. *Icarus* 89:26–43.

McBreen B. and Hanlon L. 1999. Gamma-ray bursts and the origin of chondrules and planets. *Astronomy & Astrophysics* 351:759–765.

McDonough W. F. and Sun S.-S. 1995. The composition of the Earth. *Chemical Geology* 120:223–253.

McKeegan K. D., Leshin L. A., Russell S. S., and MacPherson G. J. 1998. Oxygen isotopic abundances in calcium-aluminum-rich inclusions from ordinary chondrites: Implications for nebular heterogeneity. *Science* 280:414–418.

McKeegan K. D., Aléon J., Bradley J., Brownlee D., Busemann H., Butterworth A., Chaussidon M., Fallon S., Floss C., Gilmour J., Gounelle M., Graham G., Guan Y., Heck P. R., Hoppe P., Hutcheon I. D., Huth J., Ishii H., Ito M., Jacobsen S. B., Kearsley A., Leshin L. A., Lui M.-C., Lyon I., Marhas K., Marty B., Matrajt G., Meibom A., Messenger S., Mostefaoui S., Mukhopadhyay S., Nakamura-Messenger K., Nittler L., Palma R., Pepin R. O., Papanastassiou D. A., Robert F., Schlutter D., Snead C. J., Stadermann F. J., Stroud R., Tsou P., Westphal A., Young E. D., Ziegler K., Zimmermann L., and Zinner E. 2006. Isotopic compositions of cometary matter returned by Stardust. *Science* 314:1724.

McKeegan K. D., Kalio A. P. A., Heber V. S., Jarzebinski G., Mao P. H., Coath C. D., Kunihiro T., Wiens R. C., Nordholt J. E., Moses R. W. Jr, Reisenfeld D. B., Jurewicz A. J. G., and Burnett D. S. 2011. The oxygen isotopic composition of the Sun inferred from captured solar wind. *Science* 332:1528–1532.

McSween H. Y. Jr. 1987. Aqueous alteration in carbonaceous chondrites: Mass balance constraints on matrix mineralogy. *Geochimica et Cosmochimica Acta* 51:2469–2477.

McSween H. Y. and Richardson S. M. 1977. The composition of carbonaceous chondrite matrix. *Geochimica et Cosmochimica Acta* 41:1145–1161.

Melosh H. J. 1996. *Impact cratering: A geologic process.* New York: Oxford University Press. 245 pp.

Nesvorný D., Jenniskens P., Levison H. F., Bottke W. F., Vokrouhlicky D., and Gounelle M. 2010. Cometary origin of the zodiacal cloud and carbonaceous micrometeorites: Implications for hot debris disks. *The Astrophysical Journal* 713:816–836.

Radomsky P. M. and Hewins R. H. 1990. Formation conditions of pyroxene-olivine and magnesian olivine chondrules. *Geochimica et Cosmochimica Acta* 54:3475–3490.

Reshma K., Rudraswami N. G., and Prasad M. S. 2013. Chondrule-like object from the Indian Ocean cosmic spherules. *Journal of Earth System Science* 122:1161–1171.

Richardson S. M. 1981. Alteration of mesostasis in chondrules and aggregates from three C2 carbonaceous chondrites. *Earth and Planetary Science Letters* 52:67–75.

Rochette P., Folco L., Suavet C., Van Ginneken M., Gattacceca J., Perchiazzi N., Braucher R., and Harvey R. P. 2008. Micrometeorites from the Transantarctic

Mountains. *Proceedings of the National Academy of Sciences of the United States of America* 105:18,206–18,211.

Rubin A. E. 1991. Euhedral awaruite in the Allende meteorite: Implications for the origin of awaruite- and magnetite-bearing nodules in CV3 chondrites. *American Mineralogist* 76:1356–1362.

Rubin A. E. 2000a. Physical properties of chondrules in different chondrite groups: Implications for multiple melting events in dusty environments. *Geochimica et Cosmochimica Acta* 74:4807–4828.

Rubin A. E. 2000b. Petrologic, geochemical and experimental constraints on models of chondrule formation. *Earth Science Reviews* 50:3–27.

Rubin A. E. and Grossman J. N. 2010. Meteorite and meteoroid: New comprehensive definitions. *Meteoritics & Planetary Science* 45:114–122.

Rudraswami N. G., Genge M. J., Marrocchi Y., Villeneuve J., and Taylor S. 2020. The oxygen isotope compositions of large numbers of small cosmic spherules: Implications for their sources and the isotopic composition of the upper atmosphere. *Journal of Geophysical Research: Planets* 125: e2020JE006414.

Sanders I., and Scott E. R. D. 2012. The origin of chondrules and chondrites: Debris from low-velocity impacts between molten planetesimals? *Meteoritics & Planetary Science* 47:2170–2192.

Schrader D. L., Davidson G., and McCoy T. J. 2016. Widespread evidence for high-temperature formation of pentlandite in chondrites. *Geochimica et Cosmochimica Acta* 189:359–376.

Scott E. R. D. 1988. A new kind of primitive chondrite, Allan Hills 85085. *Earth and Planetary Science Letters* 91:1–18.

Scott E. R. D., Love S. G., and Krot A. N. 1996. Formation of chondrules and chondrites in the protoplanetary nebula. In *Chondrules and the protoplanetary disk*, edited by Hewins R. H., Jones R. H., and Scott E. R. D. Cambridge: Cambridge University Press. pp. 87–96.

Shu F. H., Shang H., and Lee T. 1996. Towards an astrophysical theory of chondrites. *Science* 271:1545–1552.

Suavet C., Alexandre A., Franchi I. A., Gattacceca J., Sonzogni C., Greenwood R. C., Folco L., and Rochette P. 2010. Identification of the parent bodies of micrometeorites with high-precision oxygen isotope ratios. *Earth and Planetary Science Letters* 293:313–320.

Suavet C., Rochette P., Kars M., Gattacceca J., Folco L., and Harvey R. P. 2011. Statistical properties of the Transantarctic Mountains (TAM) micrometeorite collection. *Polar Science* 3:100–109.

Suganuma Y., Miura H., Zondervan A., and Okuno J. 2014. East Antarctic deglaciation and the link to global cooling during the Quaternary: Evidence from glacial geomorphology and 10Be surface exposure dating of the Sør Rondane Mountains, Dronning Maud Land. *Quaternary Science Reviews* 97:102–120.

Suttle M. D., Genge M. J., Salge T., Lee M. R., Folco L., Góral T., Russell S. S., and Lindgren P. 2019a. A microchondrule-bearing micrometeorite and comparison with microchondrules in CM chondrites. *Meteoritics & Planetary Science* 54:1303–1324.

Suttle M. D., Folco L., Genge M. J., Russell S. S., Najorka J., and Van Ginneken M. 2019b. Intense aqueous alteration on C-type asteroids: Perspectives from giant fine-grained

micrometeorites. *Geochimica et Cosmochimica Acta* 245:352–373.

Suttle M. D., Dionnet Z., Franchi I. A., Folco L., Greenwood R. C., Gibson J., Rotundi A., King A., and Russell S. S. 2020. Isotopic and textural analysis of giant unmelted micrometeorites—Identification of new material from intensely altered $^{16}$O-poor water-rich asteroids. *Earth and Planetary Science Letters* 546:116444. https://doi.org/10.1016/j.epsl.2020.116444.

Taylor S. and Brownlee D. E. 1991. Cosmic spherules in the geological record. *Meteoritics* 26:203–211.

Taylor S., Lever J. H., and Harvey R. P. 2000. Numbers, types, and compositions of an unbiased collection of cosmic spherules. *Meteoritics & Planetary Science* 35:651–666.

Taylor S., Alexander C. M. O'D., Delaney J., Ma P., Herzog G. F., and Engrand C. 2005. Isotopic fractionation of iron, potassium, and oxygen in stony cosmic spherules: Implications for heating histories and sources. *Geochimica et Cosmochimica Acta* 69:2647–2662.

Taylor S., Herzog G. F., and Delaney J. S. 2007. Crumbs from the crust of Vesta: Achondritic cosmic spherules from the South Pole water well. *Meteoritics & Planetary Science* 42:223–233.

Taylor S., Alexander C. M. O'D., and Wengert S. 2008. Rare micrometeorites from the South Pole, Antarctica (abstract #1628). 39th Lunar and Planetary Science Conference. CD-ROM.

Taylor S., Matrajt G., and Guan Y. 2012. Fine-grained precursors dominate the micrometeorite flux. *Meteoritics & Planetary Science* 47:550–564.

Thiemens M. H., Jackson T., Zipf E. C., Erdman P. W., and Van Egmond C. 1995. Carbon dioxide and oxygen isotope anomalies in the mesosphere and stratosphere. *Science* 270:969–972.

Tomeoka K. and Buseck P. R. 1985. Indicators of aqueous alteration in CM carbonaceous chondrites: Microtextures of layered minerals containing Fe, S, O and Ni. *Geochimica et Cosmochimica Acta* 55:943–954.

Tomeoka K., Kiriyama K., Nakamura K., Yamahana Y., and Sekine T. 2003. Interplanetary dust particles from the explosive dispersal of hydrated asteroids by impacts. *Nature* 423:60–62.

Toppani A. and Libourel G. 2003. Factors controlling compositions of cosmic spinels: Application to atmospheric entry conditions of meteoritic materials. *Geochimica et Cosmochimica Acta* 67:4621–4638.

Toppani A., Libourel G., Engrand C., and Maurette M. 2001. Experimental simulation of atmospheric entry of micrometeorites. *Meteoritics & Planetary Science* 36:1377–1396.

Van Ginneken M., Folco L., Cordier C., and Rochette P. 2012. Chondritic micrometeorites from the Transantarctic Mountains. *Meteoritics & Planetary Science* 47:228–247.

Van Ginneken M., Genge M. J., Folco L., and Harvey R. P. 2016. The weathering of micrometeorites from the Transantarctic Mountains. *Geochimica et Cosmochimica Acta* 179:1–31.

Van Ginneken M., Gattacceca J., Rochette P., Sonzogni C., Alexandre A., Vidal V., and Genge M. J. 2017. The parent body controls on cosmic spherule texture: Evidence from the oxygen isotopic compositions of large micrometeorites. *Geochimica et Cosmochimica Acta* 212:196–210.

Van Schmus W. R. and Wood J. A. 1967. A chemical-petrologic classification for the chondritic meteorites. *Geochimica et Cosmochimica Acta* 31:747–765.

Wasson J. T. 1993. Constraints on chondrule origins. *Meteoritics* 28:14–28.

Weidenschilling S. J. 2000. Formation of planetesimals and accretion of the terrestrial planets. *Space Science Reviews* 92:295–310.

Weisberg M. K., Prinz M., Clayton R. N., Mayeda T. K., Grady M. M., Franchi I. A., Pillinger C. T., and Kallemeyn G. W. 1996. The K (Kakangari) chondrite grouplet. *Geochimica et Cosmochimica Acta* 60:4253–4263.

Weisberg M. K., Prinz M., Clayton R. N., Mayeda T. K., Sugiura N., Zashu S., and Ebihara M. 2001. A new metal-rich chondrite grouplet. *Meteoritics & Planetary Sciences* 36:401–418.

Weisberg M. K., McCoy T. J., and Krot A. N. 2006. Systematics and evaluation of meteorite classification. In *Meteorites and the early solar system II*, edited by Lauretta D. S. and McSween H. Y. Tucson, Arizona: The University of Arizona Press. pp. 19–52.

Wurm G., Teiser J., Bischoff A., Haack H., and Roszjar J. 2010. Experiments on the photophoretic motion of chondrules and dust aggregates—Indications for the transport of matter in protoplanetary disks. *Icarus* 208:482–491.

Yada T., Nakamura T., Noguchi T., Matsumoto N., Kusakabe M., Hiyagon H., Ushikubo T., Sigiura N., Kojima H., and Takaoka N. 2005. Oxygen isotopic and chemical compositions of cosmic spherules collected from the Antarctic ice sheet: Implications for their precursor materials. *Geochimica et Cosmochimica Acta* 69:5789–5804.

Young E. D. and Russell S. S. 1998. Oxygen reservoirs in the early solar nebula inferred from an Allende CAI. *Science* 282:425–455.

Yu Y. and Hewins R. H. 1998. Transient heating and chondrule formation evidence from Na loss in flash heating simulation experiments. *Geochimica et Cosmochimica Acta* 62:159–172.

Yurimoto H., Krot A. N., Choi B. G., Aléon J., Kunihiro T., and Brearley A. J. 2008. Oxygen isotopes of chondritic components. *Reviews in Mineralogy and Geochemistry* 68:141–186. https://doi.org/10.2138/rmg.2008.68.8.

Zekollari H., Goderis S., Debaille V., van Ginneken M., Gattacceca J., ASTER Team, Jull A. J., Lenaerts J., Yamaguchi A., Huybrechts P., and Claeys P. 2019. Unravelling the high-altitude Nansen blue ice field meteorite trap (East Antarctica) and implications for regional palaeo-conditions. *Geochimica et Cosmochimica Acta* 248:289–310.

Zolensky M., Barrett R., and Brownlee L. 1993. Mineralogy and composition of matrix and chondrule rims in carbonaceous chondrites. *Geochimica et Cosmochimica Acta* 57:3123–3148.

## SUPPORTING INFORMATION

Additional supporting information may be found in the online version of this article.

**Data S1.** Major and minor elemental oxide concentrations (wt%) according to individual EPMA spot analyses in a single, coarse-grained olivine crystal.

**Data S2.** Major and minor elemental oxide concentrations (wt%) according to individual EPMA spot analyses in a single, coarse-grained low-Ca pyroxene crystal.

**Data S3.** Major and minor elemental oxide concentrations (wt%) of individual EPMA spot analyses in the spherical inclusion.

**Data S4.** Major and minor elemental concentrations (wt%) according to individual EPMA spot analyses in a series of Fe-Ni metallic nodules and sulfides.

**Data S5.** Oxygen isotope ratios ($\delta^{17}O$, $\delta^{18}O$, $\Delta^{17}O$) of major components within the micrometeorite WF1202A-001, including the spherical inclusion (SI), the groundmass (GM), and refractory silicates (olivine and low-Ca pyroxene).

**Data S6.** Additional images of mineral constituents in micrometeorite WF1202A-001, including the spherical inclusion (A), a resorbed olivine grain (B), the micrometeorite rim containing newly formed Fe-oxide phases (C), and a close-up of the largest low-Ca pyroxene grain with FeO-rich olivine overgrowth (D).